Energy 274 (2023) 127303

Contents lists available at ScienceDirect

Energy

journal homepage: www.elsevier.com/locate/energy

The impact of mineral compositions on hydrate morphology evolution and phase transition hysteresis in natural clayey silts

Hang Bian [a,b], Xuwen Qin [c,d,e], Jinsheng Sun [f,g], Wanjing Luo [a,**], Cheng Lu [b,d,e], Jian Zhu [h], Chao Ma [d,e], Yingfang Zhou [a,i,*]

[a] School of Energy Resources, China University of Geosciences, Beijing, 100083, China
[b] Center of Oil & Natural Gas Resource Exploration, China Geological Survey, Beijing, 100083, China
[c] China Geological Survey, Beijing, 100083, China
[d] Guangzhou Marine Geological Survey, China Geological Survey, Guangzhou, 510075, China
[e] National Engineering Research Center of Gas Hydrate Exploration and Development, Guangzhou, 511458, China
[f] China University of Petroleum (East China), Qingdao, 266580, China
[g] CNPC Engineering Technology R&D Company Limited, Beijing, 102206, China
[h] iRock Technologies, Beijing, 100094, China
[i] School of Engineering, University of Aberdeen, UK

ARTICLE INFO

Handling Editor: Wojciech Stanek

Keywords:
Clayey silt
Hydrate phase transition
Micro-scale properties
Micro-scale imaging

ABSTRACT

Natural gas hydrate is a clean and high-efficient energy resource, and more than 90% of its reserves are contained in fine-grained (typically clayey silts) sediment. In this work, for the first time, the micro-scale imaging is performed to explore hydrate phase transition, morphology evolution and fundamental characteristics (mineral compositions, pore structures and seepage capacity) in clayey silt sediments. The results indicate that clayey silts formation properties strongly depend on dominant minerals component in the sediments. The clay-rich clayey silt possesses more microcapillary interstice with smaller permeability than that in quartz-rich sediment. Hydrates generally occur as microfracture-filling (veins) and grain-displacing (nodulus) in sand-rich clayey silt. While they occur in the form of fracture-filling (vein) and foraminifera-filling in clay-rich clayey silt sediments. Biological fossils (especially foraminifera) provides potential space for hydrate aggregates. But hydrate formed inside it depends on the structures of fossils, the mineral components and pore structure of surrounding matrix. The hysteresis between hydrate formation and decomposition found to be more significant in clay-rich clayey silt sediment than quartz-rich sediment. And this hysteresis inside foraminifera is much more serious compared with that in matrix. In addition, dispersed pore-filling hydrates forms during decomposition, which has adverse effect on continuous gas production.

1. Introduction

Under the background of economic globalization, the global energy consumption is projected to increase in the coming years [1]. However, carbon emission from the conventional fossil fuels has led to increasing environmental concern and global warming, which becomes an imminent consideration [2]. NGH is crystalline solid, in which guest gas molecules are trapped in host water cavities [3]. NGH is widely distributed in continental permafrost and marine sediments, and it is considered as an environmental-friendly alternative energy resource compared with other fossil fuels [4]. The estimated global natural hydrate reserve is twice of that in combined conventional fossil fuels [3]. The promising prospect has arisen great interests of energy consuming countries in recent years and many of them have carried out geological explorations [5] or pilot field tests [6]. According to statistics, hydrate in clayey silt sediments contains more than 90% of the total NGH resources in the world [7,8]. Typical clayey-silt hydrate reservoirs are globally distributed, including the Ulleung Basin in Korea [9], the northern part of the South China Sea [10], the Gulf of Mexico [11,12], the Cascadia Margin [13], the offshore Peru [14,15] and the K-G Basin in India [16], etc.

Thoughtful understanding of hydrate formation and decomposition

* Corresponding author. School of Energy Resources, China University of Geosciences, Beijing, 100083, China.
** Corresponding author.
E-mail addresses: luowanjing@cugb.edu.cn (W. Luo), Yingfang.zhou@abdn.ac.uk (Y. Zhou).

https://doi.org/10.1016/j.energy.2023.127303
Received 8 September 2022; Received in revised form 13 March 2023; Accepted 21 March 2023
Available online 27 March 2023

process, such as hydrate morphology, hydrate phase transition and the evolution of them can provide strong theoretical support for better NGH development. The attenuation of P- and S-waves and change of conductivity during seismic exploration and resource assessment are directly governed by hydrate structure and saturation in NGH reservoir [17–22]. In addition, the physical properties of hydrate-bearing sediments, such as thermal conductivity [23], intrinsic permeability [24] and mechanical strength [25] are also dominated by the specific distribution of hydrates in porous medium.

With the recent development of imaging technologies, micro-CT has been widely used as a nondestructive instrument to observe the inner structure of hydrate-bearing samples [26]. Numerous scholars have conducted research on hydrate formation and decomposition process based on CT technology. For hydrate formation, most of the scholars [27–30] found that hydrates preferentially developed at gas-water interface. Hydrates possess irregular microstructures [30], and the nucleation and distribution of hydrates are heterogeneous at grain scale as well as sample scale [28,31,32]. The distribution and migration of gas and water phases dominate the subsequent growth direction [31] and surface morphology of hydrates [28,31]. Specifically, Lei et al. [33] indicated that hydrate tended to adopt round and smooth surfaces when in contact with water, while exhibited angular interfaces when in contact with gas. Moreover, gas occurrence types can also alter hydrate occurrences [34].

For hydrate decomposition, some scholars indicated that hydrate decomposition started at the hydrate-gas interface, not at the contacts with quartz grains [6,35]. Gupta et al. [36] confirmed the characteristic of radial dissociation of hydrates. The different changing rate of hydrate surface area at different decomposition stages suggests that hydrate morphology will change during decomposition [37]. Some scholars indicated that this hydrate morphology transition is caused by the change of the distribution of decomposed water [35] and the limited diffusion of gas in water phase [38]. Moreover, hydrate re-formation was likely to occur during initial decomposition process [35]. And water saturation was the dominant factor of hydrate re-formation site [39]. Meanwhile the hydrate re-formation may promote homogeneous distribution of hydrate in pores [6].

The distinction between different hydrate habits (cementing or non-cementing) was initially deduced from the effect of hydrate morphologies on elastic wave velocity [40]. Several idealistic theoretical models (including pore-filling, grain-cementing, grain-coating, load-bearing and patchy) for pore habits of laboratory-synthesized hydrates in porous medium have been proposed in previous literatures [41–45]. Some researchers have conducted the studies on hydrate pore habits evolution based on micro-CT technology. Results show that different hydrate formation conditions (such as excess-gas and excess-water) can lead to different evolution rules of hydrate habits [31,33]. Mass and heat transfer during hydrate formation can also lead to habit transformation.

However, it is worth noting that the above-mentioned studies were conducted in large size (hundreds to thousands of microns) glass beads or quartz sand, which are the experimental substitutes of coarse-grained hydrate sediments. These materials are enormously different from the natural fine-grained clayey silt hydrate sediments in mineral composition, particle size distribution, types of porous space and seepage capacity. The natural clayey silt hydrate sediments possess typical characteristics of tight reservoirs, including extremely small pore size, low porosity and ultra-low permeability [46]. Numerous field coring data indicate that hydrates in coarse-grained sediments basically show the same hydrate occurrence as those observed in large-grained glass beads or quartz sands in laboratory tests. While the hydrate occurrences in fine-grained sediments (typically clayey silts) mainly show in grain-displacing occurrence (including fracture-filling/veins, chunks/-nodules and lenses types), which are significantly different from those in coarse-grained sediments [47,48]. The essence of the difference is that further hydrate growth mostly proceeds by invading adjacent pores in coarse-grained sediment when hydrate growth is restricted by mineral particles; While in fine-grained sediment, further hydrate growth is mainly achieved by replacing particles to enlarge the occupied pores [41]. It is mainly caused by the relative balance between the effective stress and the hydrate-water capillarity in sediments with difference particle sizes. Capillary force prevails in fine-grained sediment, so that hydrate is easier to replace particles than to invade into small throats. The pore throat size of coarse sediment is much larger and the capillary force is insignificant. Therefore, hydrate is more inclined to invade the adjacent pores under high effective stress [41].

By far, there has been limited lab study on hydrates in natural clayey silt at micro-scale. Wu et al. observed hydrate occurrences in silty sediment and discussed mechanical properties of hydrate-bearing clayey silt by self-developed CT triaxial apparatus [49]. Liu et al. [50] conducted nano-CT scanning on samples from Shenhu area in the South China Sea and found that clayey silts are usually rich in foraminifera, which increases pore space of sediments. Liu et al. [51] performed X-CT scanning on natural hydrate-bearing clayey silt pressure-core at low-temperature and high-pressure condition. Results indicated that there were only bulk hydrates formed in clayey silt without bio-fossils, and no dispersed hydrates were found in matrix pores. Li et al. [52] synthesized hydrate in foraminifera and demonstrated that liquid and gas migrated into the shells through through-holes and hydrates directly contacted inner wall of foraminifera. At present, there is few research on evolution of hydrate occurrences in fine-grained sediments, and even less research on the characteristics of hydrate phase transition in such sediments.

The overall aim of this work is to investigate the characteristics of hydrate phase transition and morphology evolution in clayey silts. Two representative clayey silts with different dominant minerals collected from the hydrate reservoir in the South China Sea are selected by quantitative characterization through QEMSCAN technology. Quantitative characterizations of particle size, pore space and seepage capacity are performed based on the obtained multi-scale spatial structures of samples by SEM and micro-CT scanning techniques. Similar to the previous study [53], xenon is utilized as a substitute of methane to generate hydrate in this study. Hydrate phase transition experiments in natural clayey silts are successfully performed by using stepwise pressurization and depressurization methods for the first time. The pore-scale distribution and morphology evolution of hydrate at typical states during formation and decomposition are captured. The decisive effect of mineral compositions on the phase transition properties and morphology evolutions has been discussed contrastively. The results of this research are the theoretical basis of studies on evolution characteristics of seepage capacity and mechanical properties during hydrate phase transition in clayey silts. In addition, the results possesses guiding significance to the production tests of clayey silt hydrate-bearing reservoirs.

2. Sample preparation and methodology

2.1. Dry scan of clayey silt samples

As observed in the field, the contents of silt and clay vary significantly in different fine-grained NGH sediments. For example, the overall sand content is lower in the K-G basin of India, but some high-concentrated sand regions can still be observed [54]. In Ulleung Basin, mineral contents of the sandy clay sediment are different from those in the clay-dominant fine-grained sediments [55]; and there are many microfossils dispersing in clay minerals in the clay-dominant sediments. In the South China Sea, the sand content in clayey silt sediment of Qiong Dongnan area is higher than that of Shenhu area [56,57]. While the clay content of the sediments in the offshore Peru, the Gulf of Mexico and the Cascadia Margin are generally dominant [41]. Previous work also suggests classifying the fine-grained NGH sediments into three main lithofacies with distinct grain size distributions (type-A-silty clay to clayey silt, Type B-clayey silt and Type C-sandy silt to silty sand), indicating

that grain size increases with the decrease of clay content [58]. And thus, two typical samples (clay-rich and sand-rich clayey silt natural hydrate sediments) were selected as example to analyze the hydrate occurrence evolution in clayey silt hydrate reservoir. Before phase transition experiments, the two samples are scanned by several methods to provide basic images for the subsequent qualitative and quantitative characterization of physical properties including mineralogy, pore space and seepage capacity. The specific preparation process of SEM samples is detailed in Appendix A.

MAPS imaging. Scanning electron microscope (SEM) is an instrument for high-resolution imaging of materials [59]. The electrons interact and scatter as impacting various minerals. SEM images can be obtained by scanning the surface of specimen and mapping the intensity of corresponding scattered electrons and other energy signals [60]. The primary electrons reflected by elastic collisions, also known as backscattered electrons (BSE), is one of the main parts of the imaging signal in SEM. The electrons are converted into video signals through the detector and the SEM image can be formed after amplification and brightness adjustment.

MAPS is a modular automated processing system with automatic imaging control function. It can seamlessly stitch thousands of high-resolution SEM images together to generate a complete, multi-scale SEM image of the area of interest. In this study, MAPS images of the target areas are acquired by stitching plenty of consecutive SEM images with a resolution of 5 μm and pixel number of 2048 × 1768.

QEMSCAN imaging. QEMSCAN (Quantitative Evaluation of Minerals by Scanning electron microscopy) is a comprehensive automatic mineral detection method. QEMSCAN technology combines energy-dispersive spectroscopy (EDS) and backscattered electron (BSE) intensity from a SEM and identifies minerals by comparison with a predefined mineral database [61]. The specific descriptions are referred in the research of Gottlieb et al. [62]. In this work, a 15 kV electron beam is used to obtain 2D SEM images for quantitative analysis of minerals in a high vacuum condition. The scanning resolution is 5 μm, and the scanning area is 8 mm × 8 mm. A series of data processing is then performed, specifically including integrating several mineral phases into mineral aggregates, decomposing mixed spectra (boundary phase processing), image filtering, and particle classification.

FIB-SEM imaging. FIB-SEM (Focused Ion Beam Scanning Electron Microscopy) is the combination of SEM and focused ion beam [63,64]. Firstly, the 3D slice range and thickness (number of slices) are set. After scanned by electron beam, the sample surface is etched by the large focused ion beam and then smoothed by the small one. Subsequently, SEM scans the new sample surface [65]. This cycle continues until the sample is cut to a predetermined depth. Finally, plenty of continuous 2D images are reconstructed into 3D FIB-SEM images using reconstruction algorithm.

Micro-CT imaging. 3D internal space of samples can also be tested by micro-computed tomography (micro-CT), which is a non-destructive technology. The high-pressure chamber is fixed on the 3D detection platform, and rotates 360° for scanning [53]. The radiation emitted from X-ray source is attenuated by various phases and then received by the detector. To optimize image quality, each sample is scanned under 120 kV. By converting the attenuated X-rays into digital and electrical signals, the attenuation coefficients are acquired, and 3D gray-scale images of the samples can be subsequently obtained by 3D reconstruction algorithm [53].

2.2. Hydrate phase transition experiment

Experimental preparations. A cylinder with a length of 4 mm and a diameter of 5 mm are sampled from each of the two pieces for hydrate phase transition experiment. Xenon gas (purity of 99.999%) and the in-situ seawater produced by thawing frozen samples serve as raw materials of hydrate formation. Both methane hydrate and xenon hydrate are classified as Type I structure hydrate [66]. The similarities of the two hydrates in various aspects have been verified, including lattice structure, phase equilibrium thermodynamic, growth kinetics and mechanical properties [67–69]. In addition, the linear attenuation coefficient of xenon hydrate is much higher than that of methane hydrate [66,70], which can significantly enhance adsorption of X-rays and thus improve imaging contrast. Serious risks related to the operations with potentially explosive gas under high pressure can be greatly alleviated, since the stability pressure of xenon hydrate is much lower. In brief, xenon hydrate is a convincing substitute of methane hydrate for experimental study. Moreover, according to the latest in–situ NMR and well logging data achieved during natural gas hydrate drilling program in the Shenhu Area [71], pore space of clayey-silt hydrate reservoir is mainly filled with capillary irreducible water, followed by clay irreducible water, with almost no movable water. Thus, excess-gas method is used here to generate connate water condition in the clayey-silt hydrate reservoir.

The experimental setup (see Fig. 1) is an integrated test system composed of experimental apparatuses and micro-CT facility. Specific parameters of experimental apparatus were introduced in detail in the previous work [53]. At preparation stage, micro-CT operation is tested. The scanning resolution of sample A (clay-rich) is 5.04 μm, while it is 2.54 μm for sample B (sand-rich). Then, xenon gas is charged and discharged for several times in the chamber (loading sample) to exhaust the air.

Experimental procedures. Fig. 2 depicts pressure-temperature paths over the entire experiment with temporal distribution of micro-CT scans of clayey silts. Temperature is controlled at approximately 285.15 K (12 °C) throughout the process. Stepwise pressurization method is utilized for hydrate formation and stepwise depressurization is used during decomposition. As shown in previous studies, most of the clayey silt is unconsolidated with a labile structure [72–76]. The microstructure and fluid distribution will be influenced if a larger pressure gradient is applied, and thus a relatively small pressure gradient should be applied to avoid potential damage. Preliminary tests for hydrate formation and decomposition with different pressure gradients were carried out. Based on the results of a series of preliminary tests, the pressure gradient for hydrate formation, which can not only greatly maintain the original porous space, but also control the formation process within an appropriate period. Moreover, small gradients are also used to capture the initial pressure of hydrate phase transition for analyzing the hysteresis phenomenon (Section 3.4).

Multiple CT scans are conducted within phase transition process. The CT scan of 'Initial State' is obtained before injecting gas into the chamber, and the initial scanning time is set as time '0'. In the stage of pressure-induced hydrate formation, xenon gas is injected continuously into the chamber with initial pressure equals to 0.1 MPa and then the pressure is increased stepwise with an interval of 0.1 MPa until hydrate is formed in the sample. Hydrate formation starts when pressure increased to 1.1 MPa in sample A, to 1.0 MPa in Sample B; then second CT scan, 'P-1', is performed immediately. Subsequently, xenon gas continues to be injected into the chamber until the pressure reaches 1.5 MPa to ensure sufficient hydrate formation. CT scan 'P-2' is performed after 7 days (168 h) at this pressure-temperature state to obtain the initial fluid-hydrate-gas-solid distribution before hydrate decomposition. The pressure is then reduced stepwise with an interval of 0.1 MPa to study hydrate decomposition process. The first CT scan of hydrate decomposition process, 'DP-1', is conducted 24 h after initial hydrate decomposition (the pressure at this point of sample A is 0.6 MPa and that of sample B is 0.3 MPa). The pressure continues to drop by 0.1 MPa, and CT scan 'DP-2' is performed after keeping at this state for 24 h. This process is repeated until hydrates disappear thoroughly, and then the pressure is released as the atmosphere pressure.

2.3. Micro-scale characterization and modeling based on images

Image postprocessing. Equipment operating conditions (such as current, voltage, etc.) and instability of external conditions (such as

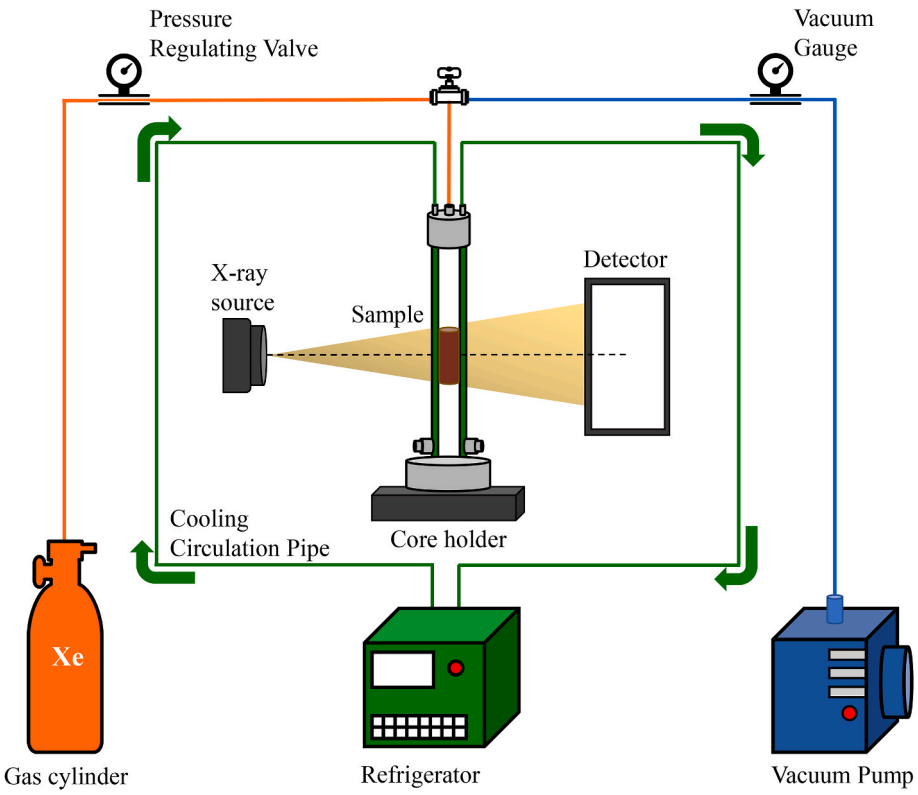

Fig. 1. Experimental setup, including micro-CT and experimental system of hydrate phase transition.

temperature and pressure) during imaging process will affect sensors and circuit elements, and therefore generate image noise. In this work, the non-local means filter [77] is utilized for 2D and 3D image denoising while preserving the original information of the image greatly. The watershed algorithm [78] is then applied for phase segmentation based on the atomic number contrast of SEM images (including 2D BSE and 3D FIB-SEM images) or on the relative radiodensity of various materials to X-rays in micro-CT images. Thus, the resulting segmented gray-scale images can be used for further micro-scale characterizations and simulations.

Minerals characterization. Through enlarging 2D MAPs images, different types of mineral grains and pore space structures at whatever positions can be clearly observed. Based on Qemscan images, minerals content of samples can be quantitatively analyzed. Therefore, not only mineralogical information, but also grain morphology, mineral embedded characteristics and elemental occurrences of the clayey silt samples can be obtained.

Particle size distribution. Minerals can be separately extracted and marked based on 2D MAPS images with high resolution. The single particle size can be calculated with the method of equivalent diameter, as shown in Eq (1),

$$E_qD = \sqrt{\frac{4 * S_{area}}{\pi}} \tag{1}$$

where E_qD denotes equivalent circular diameter, S_{area} denotes the surface area of the single particle. Finally, the particle size distribution can be statistically summarized.

Pore space characterization. Pore space characterization based on 2D MAPS images is to acquire the equivalent aperture of pores through central axis method, after which the continuous distribution of multi-scale pore size can be obtained by statistical analysis.

While based on 3D images, porosity of clayey silt samples can be calculated as the fraction of pore voxels over the total voxels. Pore size distributions are obtained by NMR simulations. NMR relaxations are simulated using the Random Walker algorithm [79,80]. Throat size distributions are obtained by performing mercury injection simulations in 3D digital models. Moreover, tortuosity of the pore space can be obtained by simulating Brownian Motion of diffusive particles (random walkers) through pore space using the Random Walker Method [81]. These methods have been described in detail in previous study [53] and will not be repeated here.

Intrinsic permeability simulation. In this study, computational fluid dynamics (CFD) simulations are performed in 3D digital models to obtain absolute permeability in one certain direction. The fluid flow in porous space is assumed to be extremely slow and incompressible. The linear Stokes Equations are solved by the finite difference method (FDM). Specific introduction was described in detail in previous work [53].

3. Results and discussions

3.1. Fundamental characteristics of clayey silts

Fig. 3 shows the backscattering SEM images of sample A and sample B with magnifying parts indicating dominant minerals and various types of pore space. The Fig. indicates that particles in both samples are randomly arranged and unconsolidated. Particle size of sample A is much finer than that of sample B. In sample A, the proportions of carbonate (basically in the form of biological fossils) and clay are relatively high. Other minerals (such as quartz, mica and feldspar, etc.) are almost tightly surrounded by clay minerals. The porous space in sample A can be classified as microfractures, biological fossil pores (mainly foraminifera), interparticle pores, and clay intercrystalline pores. Among them, biological fossil pores and clay intercrystalline pores comprise a large proportion of total porous space.

As for sample B, porous space occurs mainly in the form of large pores, interparticle macropores and clay intercrystalline pores. The proportion of biological fossil pores is much less than that of sample A.

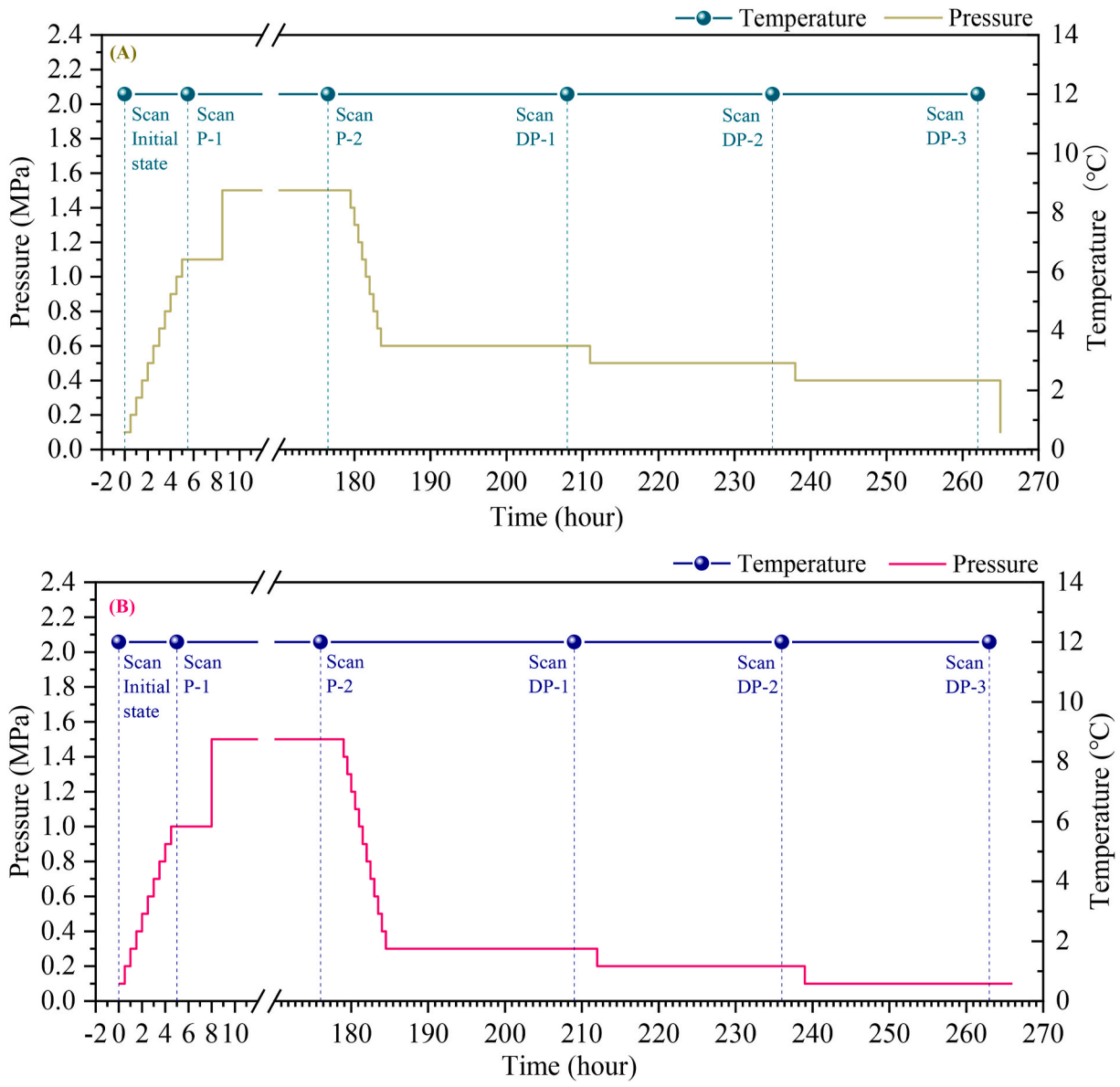

Fig. 2. The pressure-temperature path throughout phase transition experiment and the temporal distribution of micro-CT scans for sample (A) and (B) (including Initial State, P (Pressuring)-1, P-2, DP (Depressurization)-1, DP-2 and DP-3).

Particles are relatively loose-packed. Clay minerals do not totally fill the pore space among large-grained minerals, but mostly surround these minerals.

Minerals. Occurrences of particles with different shapes and dimensions in the two samples suggest complicated compositions and heterogeneous distributions of clayey silt minerals. Fig. 4 demonstrates quantitative characterization of minerals in both samples. Moreover, minerals are classified into several main types (including carbonate, clay, quartz, mica, feldspar, pyrite and others) and their proportions are shown in Fig. 4 (C). For sample A, the ratio of carbonate (mainly presenting in biological fossils) is the highest at 37.03%; the second is clay, whose content is more than a quarter of the whole; and quartz accounts for approximately 18%. While for sample B, the most abundant mineral is quartz (44.43%), and both clay and carbonate occupy approximately 16%.

According to Fig. 5, particle size range of sample A is relatively wide. The first peak of the distribution curve (A) occurs at the particle size of approximately 4 μm, which is contributed mainly by clay minerals. While the second peak occurs at the particle size of 450 μm, representing the abundant biological fossils (such as foraminifera). The distribution curve of sample B peaks when particle size reaches 40 μm, which is approximately 10 times larger than that of sample A (excluding biological fossils).

Pore space and seepage capacity. Firstly, the large-area pore size distributions of samples (Fig. 6) are obtained based on MAPS images. The radii of pores in sample A covers a wide range from submicron to submillimeter. Among them, 83.4% of the pores are submicron-scale pores. The curve peaks at 18.1% when the pore radius is 0.25 μm. Submillimeter pores are intragranular pores of biological fossils, accounting for approximately 1%. The distribution curve of pore radius in sample B peaks at 10.1% when the pore radius equals 1 μm. There is a low peak (1%) between 0.1 μm and 0.2 μm in pore radius. The number of pores with radius between 1 μm and 10 μm accounts for 55.4% of the total, and the proportion of submicron pores occupies 32.6%, which denotes that more than half of the pores in sample B are macropores or intergranular pores.

Larger-sized micron-scale and millimeter-scale pores increase the total porosity of clayey silts and provide potential space for hydrate

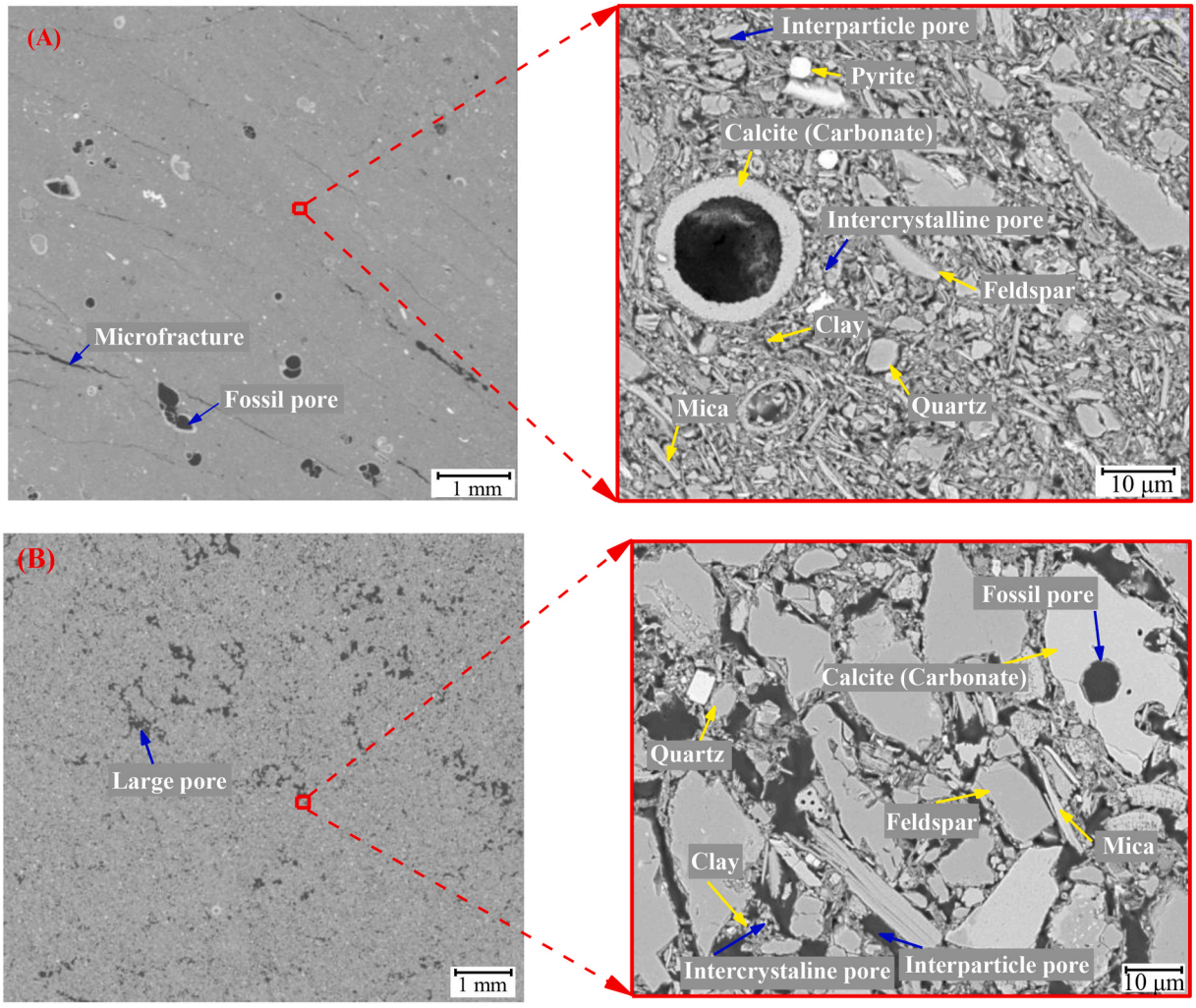

Fig. 3. MAPS images of Sample (A) and (B) with magnifying parts showing main types of minerals and pore space.

aggregates. However, plenty of submicron-scale or even nanoscale clay intercrystalline pores in silty matrix is the main factor affecting hydrate formation and seepage characteristics, which cannot be well identified at the resolution of MAPS images. Therefore, FIB-SEM scanning with a resolution of 65 nm and micro-CT scanning with a resolution of 0.95 μm are conducted respectively on silty matrix of sample A and B. Previous research shows that the selection of typical REV can promote analysis efficiency (accuracy) [82–84]. Fig. 7 shows the respective REV model of silty matrix of the two samples. Relative threshold segmentation process and gray distribution curves have been shown in Appendix B. Through size independence verification (detailed in Appendix C), the side length of the REV from clay-rich clayey silt matrix is determined to be 300 pixels, while that of the REV from quartz-rich clayey silt matrix is 500 pixels. Simulated physical parameters of pore space and seepage capacity of two sample matrix are listed in Table 1. Pore-throat size distribution curves are depicted in Fig. 8.

Table 1 demonstrates that porosity values of the silty matrix in the two samples are similar. The effective porosity accounts for more than 95% of the respective total porosity, indicating that pores in the two silty matrixes are well-connected. However, due to the high content of fine-grained minerals (mainly clay minerals) in sample A, the mean pore radius and mean throat radius are both less than 0.1 μm, which are less than one tenth of those in sample B. Combined with Table 2 [85], it can be seen from Fig. 8 that more than 70% of pores and 85% of throats in sample A matrix are categorized as microcapillary interstice. While nearly 90% of pores and more than 85% of throats in sample B matrix are classified as capillary interstice.

Moreover, tortuosity of the pore space inside silty matrix of sample A is higher and the fluid flow should be more complicated. Simulation results confirm that although porosity values of the two samples are similar, their seepage capacities differ significantly. According to Chen et al. [86], silty matrix of sample A with the permeability of far less than 0.1md belongs to tight reservoir. While permeability of that in sample B is more than 680 times that in sample A, and sample B matrix belongs to low-permeability reservoir.

3.2. *Hydrate occurrence in clayey silts*

Micro-CT images of the clay-rich clayey silt (sample A) at typical states are listed in Fig. 9. Some microfractures are randomly distributed, which makes the structure highly heterogeneous. Three of them are circled with yellow dashed box and denoted as A, B and C, respectively.

Hydrate formation in clay-rich clayey silt. At the early stage, the injected gas with the increasing pressure cannot flow into the matrix due to the ultra-low permeability of the dense clay-dominated silty matrix. Thus, xenon gas accumulates in fracture A, which is in good connectivity with the external space. Meanwhile, hydrates form rapidly along fracture sidewall. Since hydrates in fracture A are in direct and sufficient contact with gas, the water in matrix gradually diffuses to the surface of hydrate layer [87] for further hydrate formation. Both the outward migration of internal liquid and the accumulation of injected gas cause local compression of the unconsolidated sediment. As a result, fracture A

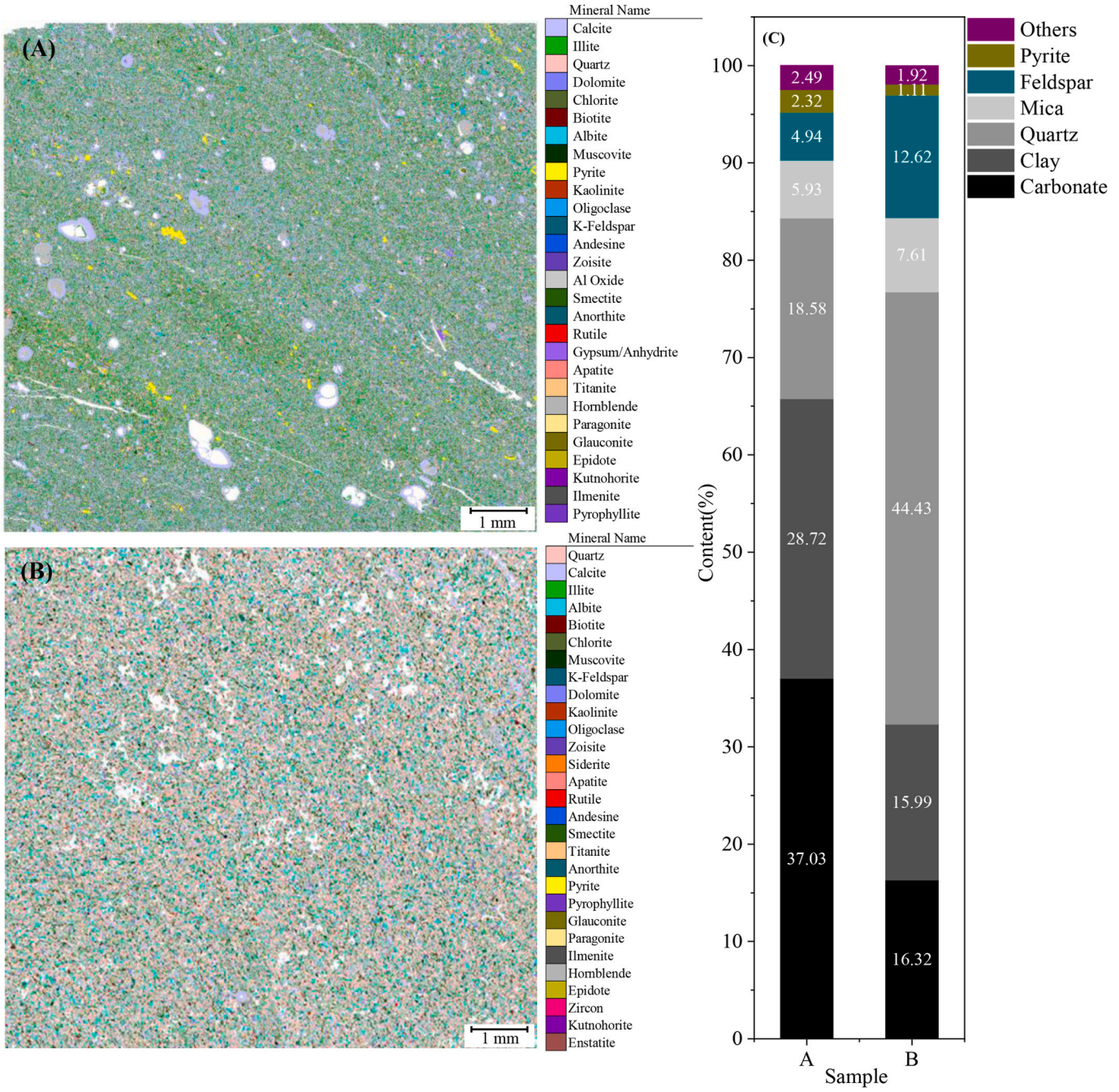

Fig. 4. (A) Qemscan image of sample A; (B) Qemscan image of sample B; (C) Proportions of main mineral categories in the two clayey silts.

is transformed into a penetrating fracture with increasing aperture (shown in the state P-1 and P-2), providing more space for hydrates. In this case, hydrates would fill the entire fracture if gas and water could be sufficient.

As for fracture B in a deeper position, the fracture aperture is similar with that of fracture A at initial state. Gas gradually invades forward till fracture B is connected with fracture C. In the meanwhile, a certain amount of hydrate is formed in B and a thin hydrate layer occurs along sidewall of C. However, the upper matrix continuously moves downward, which hinders gas from entering fracture B and impedes subsequent hydrate formation. As a result, hydrate in fracture B only shows a slight increase during later formation and the occurrence of hydrates appears as fracture-filling.

While for fracture C, the aperture is the widest at the initial state. However, due to the poor connectivity between fracture C and gas, it narrows once the pressurized gas is injected into the sample. It is not until the limited gas in fracture B breaks into fracture C that a thin hydrate layer is formed on the sidewall of C. Subsequently, hydrate formation in C is terminated due to gas supply disruption. Fracture C is continuously compressed until the previously formed hydrates fill its space.

In addition, it is difficult for gas to enter inside matrix pores due to the ultra-high capillary force caused by both microcapillary interstice and the water film surrounding clay particles. On the other hand, hydrate formation continuously extracts water from the matrix to the previously formed hydrates (microfracture-filling and foraminifera-filling in this study) and the matrix becomes compacted at the meanwhile [88]. Thus, although the direct verification is limited by the resolution of micro-CT, it should be hard to form dispersed pore-filling (embedded) hydrates in such capillary and microcapillary interstice of

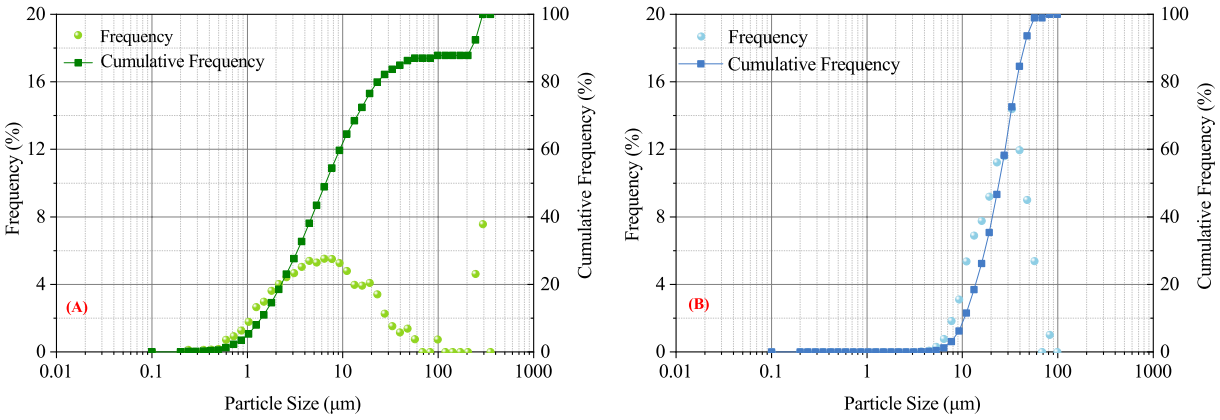

Fig. 5. Particle size distribution of sample (A) and (B) based on MAPS images.

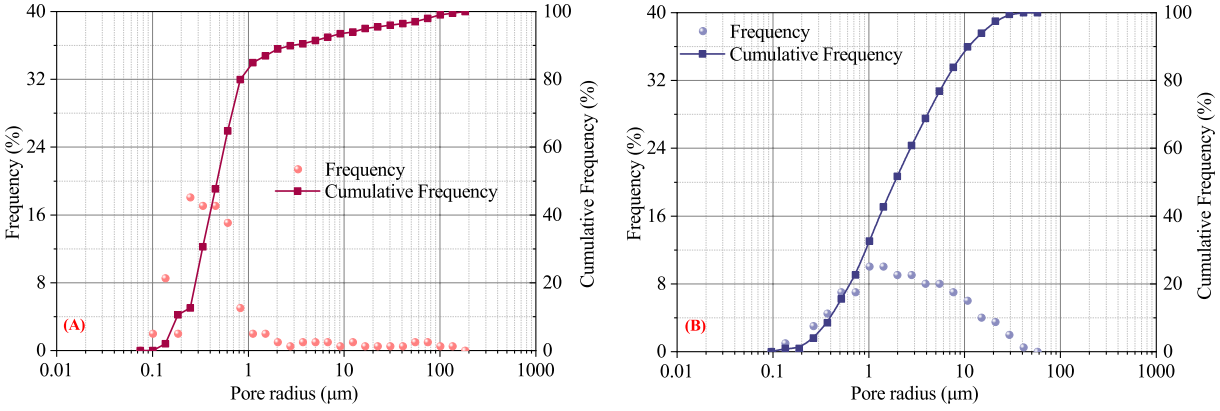

Fig. 6. Pore size distribution curves based on MAPS images of sample (A) and (B).

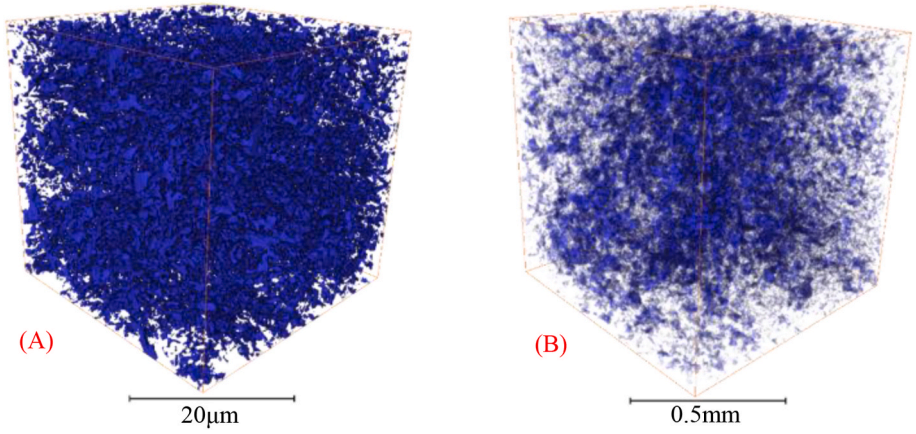

Fig. 7. The respective REV model of silty matrix in sample (A) and (B).

Table 1
Porous space and seepage characteristics of the matrix part in clayey silt samples.

Sample	Porosity [%]	Effective Porosity [%]	Permeability [md]	Tortuosity	Mean Pore Radius [μm]	Mean Throat Radius [μm]
A	16.46	15.78	0.0126	13.55	0.0998	0.0917
B	19.67	18.98	8.68	9.1	2.06	1.38

clay-dominated silty matrix. Hydrate mainly exists in the form of fracture-filling and foraminifera-filling.

Hydrate decomposition in clay-rich clayey silt. In the initial stage of depressurization (from P-2 to DP-1), hydrates in fractures remain unchanged, while those in the gap between the sample and the chamber decrease obviously. From DP-1 to DP-2, the uniformly distributed

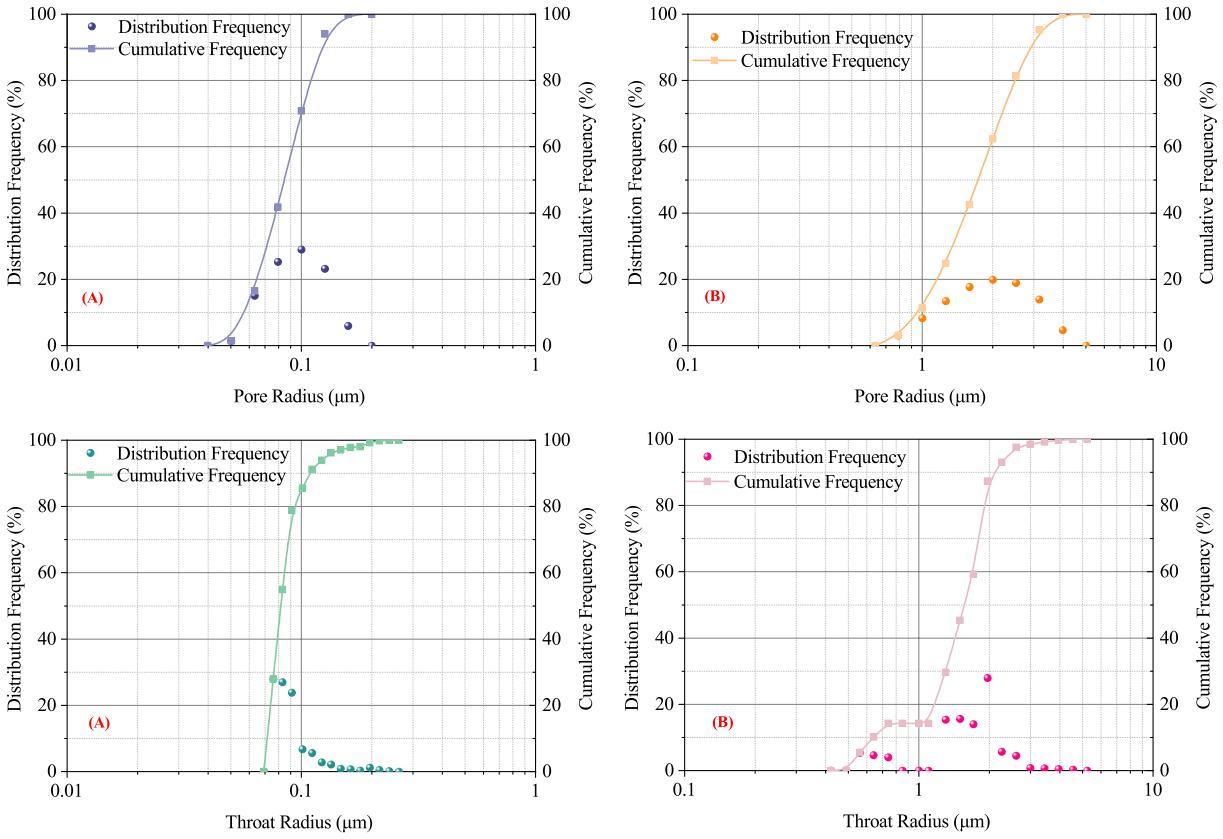

Fig. 8. Pore-throat size distributions of silty matrix in sample (A) and (B) based on 3D pore space models.

Table 2
Pore categories, respective size range and flow characteristics [85] (Φ denotes pore diameter, f_w denotes fracture width).

Pore categories	Size range [μm]	Flow Characteristics
Supercapillary interstice	$\Phi > 500$ or $f_w > 250$	Fluids can flow freely under gravity with a high flow rate or even a vortex.
Capillary interstice	$0.2 < \Phi < 500$ or $0.1 < f_w < 250$	Fluids cannot flow freely due to the capillary force. Liquids can flow inside the pores only if the external force is greater than the capillary resistance.
Microcapillary interstice	$\Phi < 0.2$ or $f_w < 0.1$	The attractive force between the fluid and the surrounding medium molecules is always extremely large, and an ultra-high pressure gradient is required for fluids migration.

hydrate layer on top of fracture A decomposes into discontinuous particles, indicating inhomogeneous hydrate decomposition. Meanwhile, the thickness of hydrate layer at the bottom slightly increases, and the volume of hydrate aggregation at the lowest position becomes larger. It is analyzed that the decomposed water of top hydrates in fracture A migrates to the bottom, and then re-form hydrates with the trapped decomposed gas [60] under local high pressure and local reduced temperature. During this period, hydrates in fracture B and C still remain undecomposed. At the final state (DP-3), hydrates in fracture A, B and C completely decomposed; however, the structure of fractures cannot recover to the initial state. Specifically, the apertures of the fractures are narrowed compared with that at the initial state, fracture A remains penetrated and fracture B is prolonged accordingly. The gap between the matrix above fracture A and the chamber wall obviously shrink, which indicates an expansion of the above matrix. It is speculated that the decomposed water absorbed into the matrix by the massive clay minerals leads to this phenomenon. However, specific distribution of decomposed water cannot be identified due to the resolution limitation of the current micro-CT technology.

Hydrate formation in quartz-rich clayey silt. Fig. 10 shows Micro-CT images of quartz-rich clayey silt (sample B) during hydrate phase transition with amplifying images of two local areas. At the initial state, sample B is loosely packed with intensively-distributed microfractures and pores inside, and no dominant channel exists between the sample and the chamber wall. In the early stage of hydrate formation (P-1), gas invades microfractures and hydrate forms at the meanwhile. From the local amplifying image at P-1, it can be seen that some microfractures (red dashed box) are completely filled with hydrates. Some hydrates displace sediment grains and occur in the form of nodulus. While other hydrate particles are scattered (blue dashed box) in microfractures and gradually connect with each other with the increasing hydrate saturation. As a result, the dispersed spheroid and discoid hydrate particles transform into vein hydrates with a greater aspect ratio. This phenomenon has also been found in the research of Wu et al. [49].

The sample is continuously squeezed downward at the same time as gas injection. The pore space where hydrates have not yet formed is compressed till the surrounding particles are tightly packed; while pores and microfractures partially occupied by hydrates are squeezed till the hydrates can support the compressed porous space. This phenomenon is consistent with the previous research that hydrate will act as the skeleton in clayey silt sediment with the increasing hydrate saturation [41, 89]. And hydrate formation in fine-grained sediment can increase the strength of sediment to some extent. Top surface of the sample gradually becomes concave with pressurization, causing further compression of matrix porous space. The previously formed hydrate deforms to some extent. Besides a few microfractures and pores well-connected with the sample-chamber gap or top gas source, most of the new-generated hydrates from P-1 to P-2 are located in the gap. This phenomenon should be caused by water migration from matrix to the gap during compression. Finally, hydrates in quartz-dominated clayey silt mainly show in

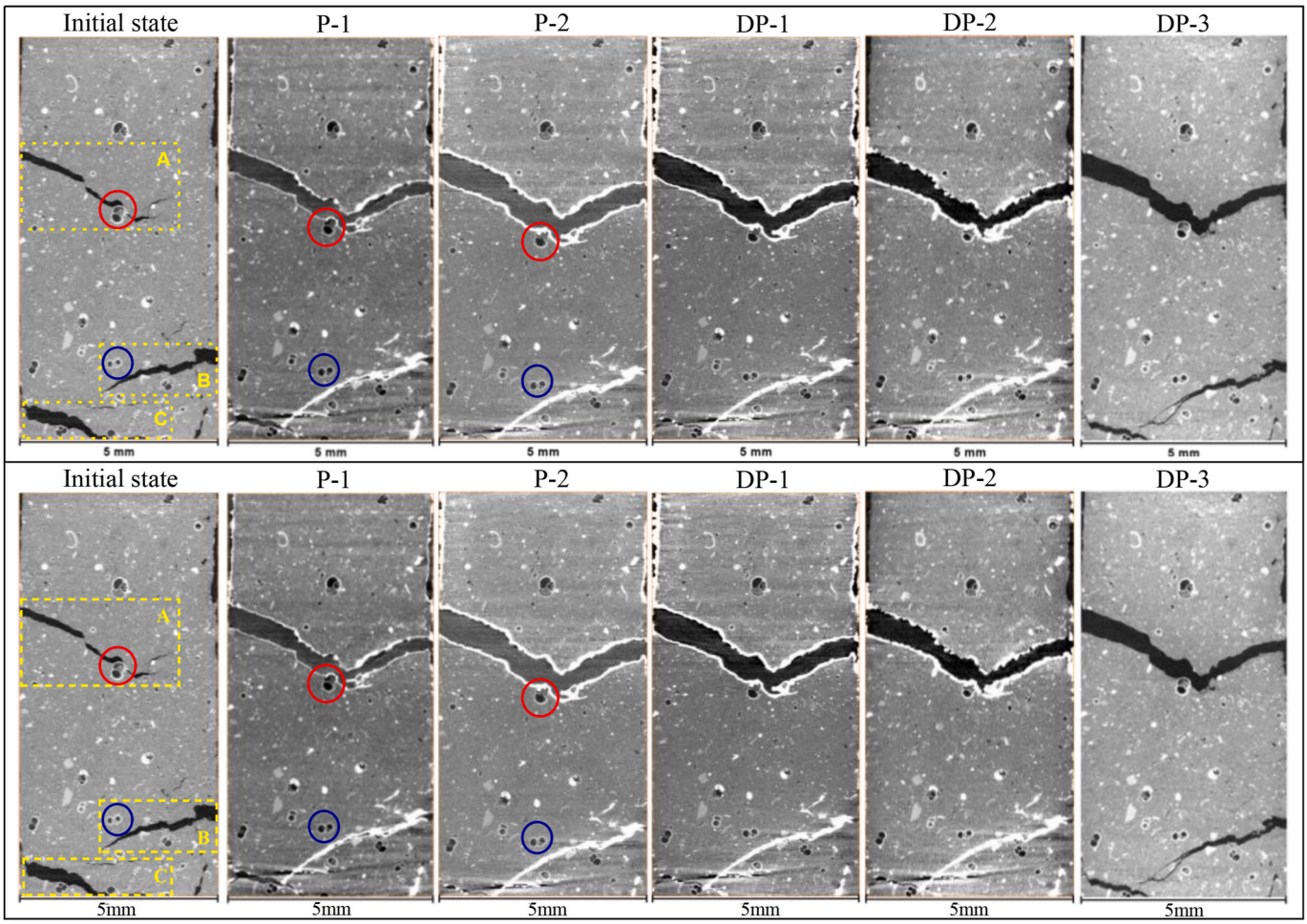

Fig. 9. Micro-CT images of sample A at different states of hydrate phase transition.

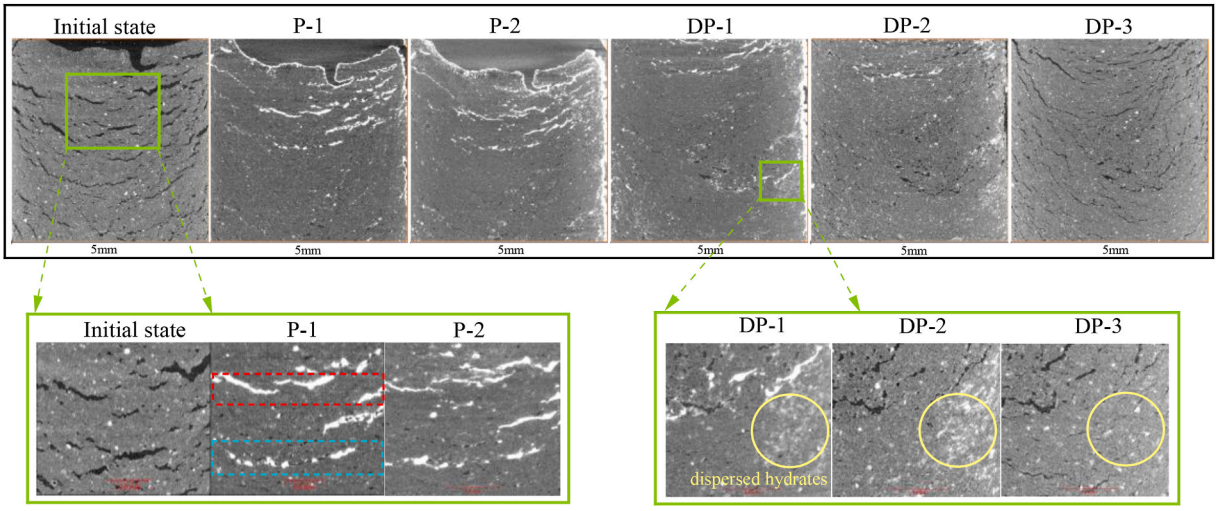

Fig. 10. Micro-CT images of sample B at different states of hydrate phase transition.

microfracture-filling (vein) and grain-displacing (nodulus) forms.

Hydrate decomposition in quartz-rich clayey silt. In the initial stage of depressurization (DP-1), decomposition starts in the chamber-sample gap and the microfractures well-connected to the external porous space. Dispersed hydrates (in yellow circles) that not present during formation occur in matrix at state DP-1. After pressure drops to DP-2 and maintains for 24 h, the dispersed hydrates do not disappear, but show a significant increase. It is analyzed that hydrates in the pore space well-connected with the outside gradually decompose with pressure decrease, throats connecting with the internal pore space become wider. Therefore, pressure is gradually transmitted to the interior of matrix, causing further hydrate decomposition. During this period, the

support cementation is significantly lost with decreasing hydrate saturation, which leads to the decrease of hardness and failure strength of clayey silt sediment [90]. The matrix gradually migrates downwards. Meanwhile, hydrates in the chamber-sample gap decompose and the sample laterally extends until it is in close contact with the chamber wall. As a result, the well-connected pore space and the dominant migration channels (chamber-sample gap) for decomposed gas and water disappear. As the matrix pores in sample B belong to the category of capillary interstice, molecular gravitational forces are always exerted between the liquid particles and between the liquid and the pore walls. High capillary force prevents internal fluids from flowing freely. The local temperature decrease caused by hydrate decomposition and the local pressure increase caused by the accumulation of decomposed gas and water lead to hydrate reformation. The reformed hydrates appear in dispersed pore-filling habits embedded in the silty matrix. The embedded type of hydrate occurrence has also been found in the research of Wu et al. [49] and Dai et al. [41]. Pressure drops further to DP-2, fracture-filling hydrates continuously decompose. The decomposed gas and water flow into matrix pores, and are still trapped under molecular gravitational force. And the conduction of external pressure drop is still hindered by high capillary force. Thus, more dispersed pore-filling hydrates occur due to local temperature decrease and pressure increase. At the final stage of depressurization, matrix gradually becomes loosely packed and hydrates decompose completely. Abundant microfractures and matrix pores reappear. However, the inside structure is significantly different from that at the initial state.

In conclusion, for clay-dominated clayey silt reservoir, fine matrix particles are densely packed. Under the ultra-high capillary force and the strong adsorption force of clay minerals on water, it is difficult for gas to enter the microcapillary interstice in matrix. In general, gas can invade forward through microfractures and the formed hydrates are in the shape of fracture-filling. As for the initial fractures with large aperture or the penetrating fractures, hydrates grow in layer on fracture sidewalls and are gradually thickened. Hydrates would fill the fracture if gas and water could be sufficient. For both cases, hydrates continuously squeeze the surrounding matrix and widen fractures during growth, leading to the damage of porous space where no hydrate formed initially. Hydrates mainly exist in the form of microfracture-filling (vein) and foraminifera-filling. While the quartz-dominated clayey silt reservoir is rich in microfractures and matrix pores. Due to the high content of pores above submicron level, the connectivity between internal porous space and gas is better. Hydrates are in the form of grain-displacing (nodulus) and microfracture-filling (vein).

During hydrate decomposition, clay-dominated clayey silt migrates downward under gravity due to the loss of support from hydrates. Consequently, sediment strength decreases, fractures are narrowed. Finally, matrix structure is significantly different from that at initial state. Likewise, hydrates dissociation in quartz-dominated clayey silt starts from the locations that is well-connected with the external porous space. During decomposition, the disappearance of dominant channels (microfractures) as well as the accumulation of decomposed water and gas can lead to an increase of pore pressure and a decrease in temperature, which can cause re-formation of dispersed hydrates in matrix pores. There still be a large amount of microfractures and matrix pores after complete hydrate decomposition. However, the aperture of most fractures is narrowed and the matrix structure differs from that at initial state.

The results possess theoretical importance for practical development of clayey silt hydrate reservoirs. Targeted reconstruction methods should be implemented for reservoirs with different mineral compositions and hydrate occurrences. Appropriate reconstruction can largely ensure productivity by reducing the transformation from fracture-filling to dispersed pore-filling (embedded) hydrate and thus the discontinuity of production in quartz-rich reservoirs, or alleviating the shrinkage or even disappearance of dominant channels for decomposed gas and water in clay-rich reservoir. Moreover, for achieving long-term development of clayey silt hydrates, thermal stimulation should be taken as a parallel measure to weaken hydrate re-formation and its adverse impacts.

Error analysis between in-situ reservoir conditions and laboratory conditions. The results shown in this section are based on xenon hydrate phase transition tests at pore scale in laboratory. Due to the better stability of xenon hydrate at lower pressure, the experiment pressure is much lower than the actual reservoir pressure (13.5 MPa) [91].

For the microstructure of clayey silt sediment, Wu et al. [49] indicate that the void ratio of clayey silt sediment can significantly decrease with the increase of formation pressure. The actual higher pore pressure can enhance cementing bonds, the ability to resist deformation [92], and also increase the elastic modulus for the pore fluid. Therefore, the failure strength of hydrate-bearing sediment is higher, and the failure volumetric strain is lower at the actual reservoir condition. As for hydrate microstructure, Lee et al. [93] demonstrate that the geometry of grain-displacing hydrate formed by filling existing fractures are mostly governed by the geometry of fracture, whereas those formed by heaving mechanisms are governed by in-situ stress conditions and geomechanical properties. Assuming an unlimited amount of methane and an unlimited time for hydrate formation, the overburden pressure is the key factor for controlling the thickness of hydrate. There is a negative relation between the thickness of hydrate and the overburden stress [94,95]. Thus, the actual hydrate thickness should be theoretically smaller than that of hydrates formed in laboratory.

3.3. Hydrate in foraminifera

Fig. 11 shows 3D distribution of foraminifera in sample A. The enrichment of foraminifera highly increases the volume of intragranular pores. According to the previous research, the high abundance of foraminifera in clayey silt is favorable for the storage and enrichment of hydrates [96,97]. Fig. 12 illustrates that the hard shell of foraminifera can keep their internal space from being compressed when unconsolidated clayey silt is deformed during hydrate formation. Some foraminifera (e.g., in the red circle in Fig. 9) are well-connected with external gas source; therefore, hydrates can be easily generated inside them. As for other foraminifera (e.g., in the blue circle in Fig. 9), clay minerals tightly wrap their outer shells due to sample deformation during pressurization. The blockage of gas channels connecting with their inner space prevents hydrate formation in these foraminifera. Therefore, whether hydrate can form inside foraminifera depends not only on their structure [98], but also on the types of minerals and matrix structure around them.

Two representative examples of hydrate phase transition inside foraminifera are listed in Fig. 12. Two pieces of hydrates in foraminifer A show as pore-filling morphology initially. Then, significant phenomenon

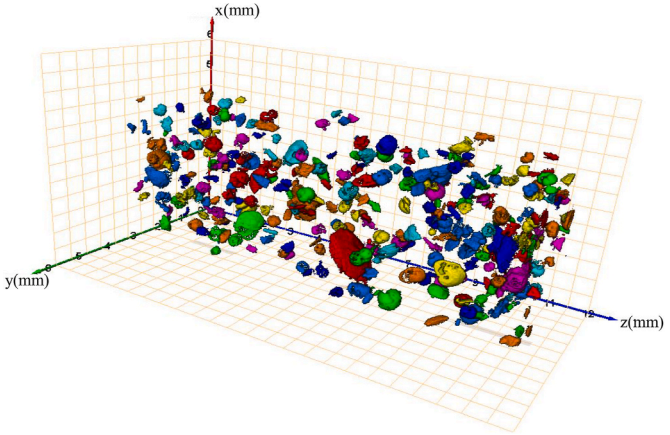

Fig. 11. 3D distributions of foraminifera containing in clayey silt sample A.

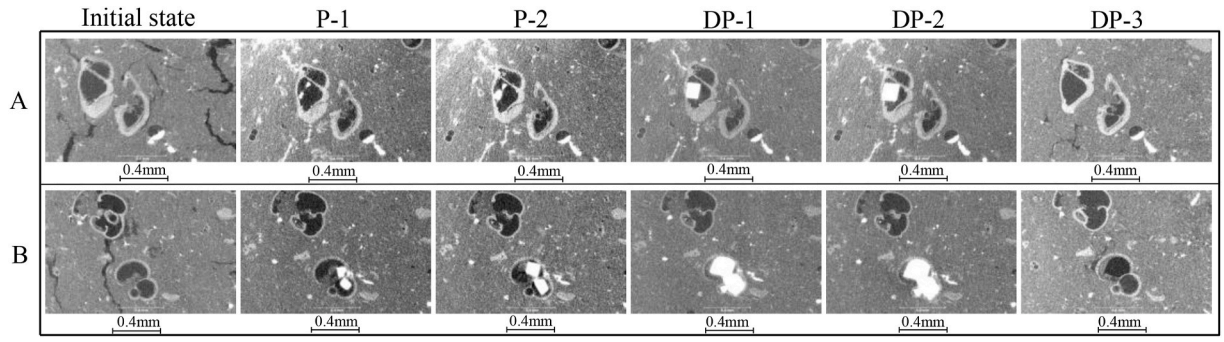

Fig. 12. Hydrate phase transition in foraminifera in sample A.

of hydrate Ostwald Ripening [99], which is generated by Gibbs-Thomson effect, is observed during process from P-1 to DP-1. That is, two pieces of hydrates merge together and gradually grow into a shape of regular cube. It should be noted that hydrate is only generated in the leftmost foraminifer. The highlighted material in the lower right circular pore should be pyrite aggregates. Likewise, there are two pieces of hydrates generated in foraminifer B. However, Ostwald Ripening phenomenon has not been observed as the two chambers in the shell are separated. Two pieces of hydrates grow as regular cubes in respective space before being confined by fossil walls. Foraminifera-filling hydrate tends to adhere to the inner walls of the shell. If time and/or gas and water source was sufficient, hydrates would fill the entire cavity. Moreover, this type of hydrate is completely surrounded by foraminifera shells, which cannot facilitate the cementation of clayey silt matrix during formation.

In addition, hydrate volume in both foraminifera A and B did not reach the highest point at pressure peak (P-2). During depressurization stage from P-2 to DP-2, hydrates inside foraminifera still continue to increase even though partial hydrates in matrix have already decomposed. In summary, foraminifera-filling hydrates in clayey silt reservoir show more significant decomposition hysteresis.

3.4. Hydrate phase transition hysteresis

During hydrate phase transition, the initial formation pressure (P-1) is found to be inconsistent with the initial decomposition pressure (DP-1) at the same temperature. As shown in Fig. 13, the pressure of P-1 of sample A is 1.1 MPa, while the pressure at DP-1 is 0.6 MPa. As for sample B, P-1 is 1.0 MPa and DP-1 is 0.3 MPa. In other words, hydrate shows the phenomenon of 'difficult to synthesize, difficult to decompose' in clayey silt. In Fig. 12, the hydrate initial formation (P-1), initial decomposition (DP-1) and final decomposition (DP-3) state points in both samples are projected on the xenon hydrate phase diagram, which is acquired in pure Xe system [100].

Hydrate formation hysteresis. Fig. 14 shows that initial formation pressures in two samples are different, but both of them are much higher than the equilibrium pressure at the same temperature. This phenomenon is supposed to be a composite effect of hydrate nucleation condition

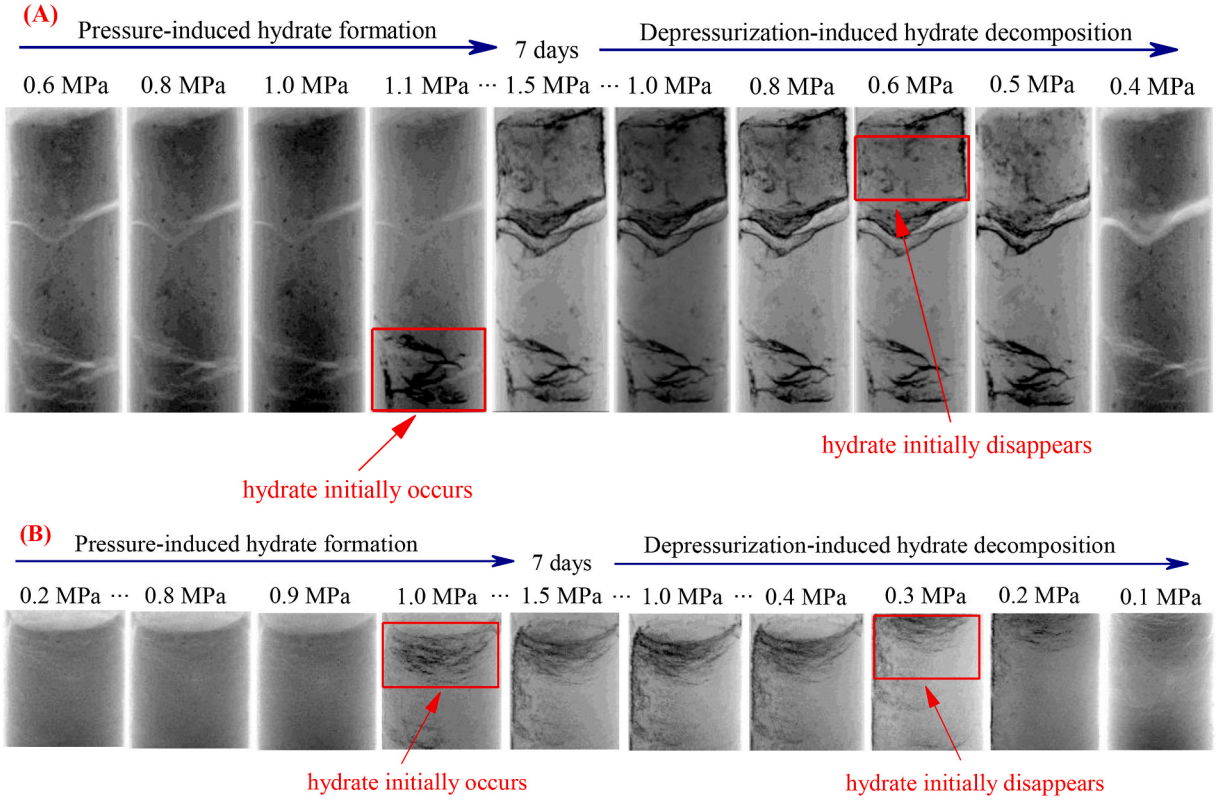

Fig. 13. Micro-CT projections during hydrate phase transition in sample (A) and (B).

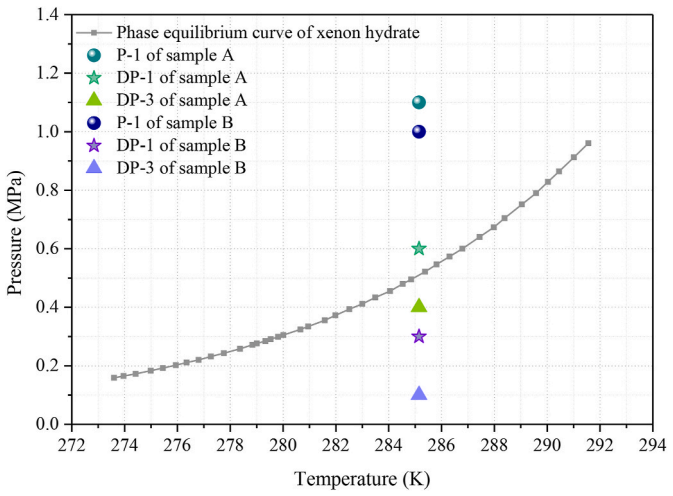

Fig. 14. Phase diagram of xenon hydrate [100] and the initial formation pressure (P-1), initial decomposition pressure (DP-1) and final decomposition pressure (DP-3) of the two clayey silt samples.

and phase boundary shift.

Firstly, when it comes to the hydrate nucleation conditions, Sloan indicated that both the gas phase and the water phase are disordered at the molecular level, whereas hydrate crystals are intrinsically ordered [3]. As entropy favors disorder over order, the initial hydrate formation is hindered by a long, metastable period (induction period). During this period, overpressure (or supercooling) as a driving force is indispensable for rearranging the disorderly gas and liquid water into the orderly hydrate crystal structure till the critical size for spontaneous growth. As shown in Fig. 15, hydrate nucleation and growth have direct analogies in crystallization processes such as the precipitation of salt from solution [3]. Mullin [101] demonstrated that (1) the right side of the equilibrium line AB is the stable region, in which crystallization is impossible; (2) the area between AB and CD is the metastable (supersaturated) region, in which spontaneous crystallization cannot occur, but if any seed exists in the metastable solution, the seed will grow; (3) the left side of CD is the unstable region, in which spontaneous crystallization can take place. A direct analogy is shown in Fig. 15 (b) for hydrates when the concentration axis of Fig. 15 (a) is replaced by a logarithmic pressure axis [3]. The AB and CD lines in Fig. 15 (b) possess the same meaning as in (a) by analogy. To the left of line CD in (b), hydrate nucleation will readily occur due to the high driving force [3]. In summary, a high driving force (overpressure in this study) is required for initial spontaneous hydrate formation in a system without hydrate seeds.

Secondly, various factors of practical clayey silt hydrate reservoirs can lead to phase boundary shift. Capillary effect of small pores can shift thermodynamic phase boundary toward lower temperature (or higher pressure), which is referred to as the Gibbs-Thomson effect [102]. Specifically, Liu et al. [103] proposed that capillary effect of pores in fine-grained quartz sand (particle size <35 μm) is so significant that temperature can be reduced by 0.5–1.5 K at the same pressure. Clennell [104] indicated that fine-grained sediments inhibit hydrate formation until the temperature is 0.5–3 °C below the equilibrium value. Clennell [104] also pointed out that strong adsorption of water by clay-rich sediments can reduce water activity and thus inhibit hydrate formation, especially at high gas saturation. Moreover, Yang et al. [105] demonstrated that saline ions in aqueous solution possess ionic effect, which can destroy ionization equilibrium, alter the equilibrium constant of hydrated ions and thus shift the phase boundary to lower temperature and higher pressure. In summary, hydrate nucleation conditions and phase boundary shift caused by various factors make the initial hydrate formation pressure significantly higher than the equilibrium value.

Furthermore, the initial hydrate formation pressure (P-1) in sample A is higher than that in sample B. According to the information in Table 2, an ultra-high pressure gradient is required for gas entering the micro-capillary interstices in sample A matrix. Moreover, it is difficult for water to flow freely as the rich clay possesses strong adsorption to water. Therefore, hydrate formation can only start when gas and water are in contact with each other through a high driving force (overpressure) and a slow diffusion process. While for sample B, microfractures are intensively distributed and sizes of matrix pores are larger. Low content of clay minerals possesses weaker adsorption to water and smaller pressure gradient is required for fluid flow in porous space. That is, the driving force required for initial hydrate formation in sample B is lower than in sample A.

Hydrate decomposition hysteresis. Hydrate decomposition should be easier and faster than hydrate nucleation, as hydrate decomposition is an entropy-increasing process. That is, ordered hydrate crystals develop into disordered gas and water. According to Sloan [3], the theoretical P-T point at which hydrates completely decompose should be infinitely approaching phase boundary. However, both the DP-3 points in Fig. 14 are beneath the phase equilibrium line. In particular, the initial decomposition pressure (DP-1) of the hydrate in sample B is located in the stable region, that is, hydrates have not start to decompose until the system pressure drops to the stable region. It seems to be contradictory with the upper shift of phase boundary during hydrate

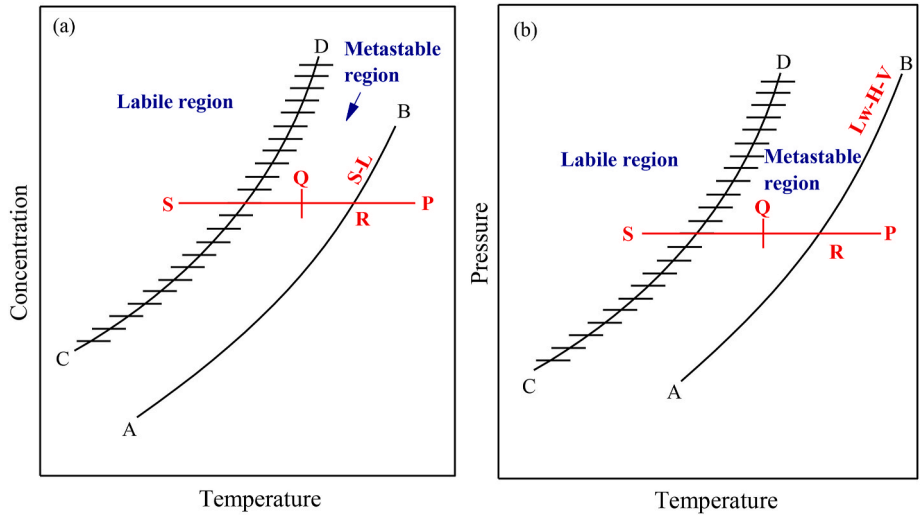

Fig. 15. (a) Crystal and (b) hydrate formation as a function of subcooling relative to the equilibrium line (AB) and the spinodal line (CD; supersaturation limit) [3].

formation. In some literatures, this unexpected high stability of hydrate at conditions out of thermodynamic equilibrium is also called 'self-preservation' effect [106,107].

According to the results in section 3.1, matrix pores of sample B are mostly capillary interstices, and hydrates mainly occur as grain-displacing (nodulus) and microfracture-filling (vein) types. Hydrate formation and creep deformation of clayey silt can lead to a dramatical reduction in porous space. The ultra-high capillary force of narrow throats hinders pressure conduction into pores. Moreover, the pore space of in-situ clay-silt hydrate reservoir is mainly filled by capillary-bound water, followed by clay-bound water, with almost no movable water [71]. Therefore, hydrates remain unchanged until the system pressure drops to a point where the internal and external pressure difference can overcome high capillary force of matrix pores and water adhesion force by clay minerals. While for sample A, hydrates occur as fracture-filling type (except those in foraminifera). The conduction of system pressure is not limited by capillary force. Decomposed water and gas can transport without the hindrance of matrix pores. Thus, initial hydrate decomposition pressure (DP-1) in sample A is higher than that in sample B, that is, hydrate in sample A is easier to decompose.

As shown in Fig. 12, foraminifera-filling hydrate is the other main type of hydrate occurrence in sample A. In the early stage of depressurization, clay minerals wrapped around foraminifera restrict pressure conduction. While in later stage, clay minerals hindered the output of decomposed water and gas. According to the results in section 3.3, foraminifera-filling hydrates show a significant decomposition hysteresis. Therefore, the final decomposition pressure (DP-3) of hydrate in sample A is below the phase boundary. For sample B, the thin throats hinder transport of decomposed gas and water, which inhibits further hydrate decomposition. Subsequently, the low temperature caused by decomposition and the high pressure caused by accumulation of gas and water result in hydrate re-formation in pores with smaller size. Thus, the system pressure required for complete hydrate decomposition in sample B is lower than that in sample A.

Different hydrate occurrences and mineral compositions of reservoirs can lead to different hysteresis degrees of hydrate phase transition. Targeted depressurization schemes should be adopted for hydrate reservoirs under different conditions. Reasonable pressure depletion together with monitoring system can largely avoid geological hazards potentially triggered by strength reduction during decomposition. The factors and relevant sensitivity analysis of hydrate decomposition hysteresis in reservoirs with inhomogeneous pore distribution and large differences in mineral contents need to be investigated in detail in the future.

4. Conclusions

In this work, hydrate phase transition experiments are performed in two clayey silts collected at different locations of hydrate reservoir in the South China Sea. The basic characteristics, including mineral compositions and porous space, are qualitatively and quantitatively analyzed. The main conclusions are as follows.

1. In clay-rich clayey silt, more than 70% of the matrix pores (except biological fossils) are microcapillary interstice. And the matrix is classified as tight reservoir ($k \approx 0.01$mD). For quartz-rich clayey silt, more than 90% of the matrix pores are capillary interstice and the matrix is low permeable ($k < 10$mD).
2. For clay-rich clayey silt, hydrates occur in the form of microfracture-filling (vein) and foraminifera-filling. While hydrates mainly exist in the form of microfracture-filling (vein) and grain-displacing (nodulus) in quartz-rich clayey silt.
3. Biological fossils (especially foraminifera) are mainly found in clay-rich clayey silt sample. Although the abundant foraminifera can provide favorable porous space for hydrate formation, the through-holes on some foraminifera shells are tightly blocked by clay minerals, which hinders hydrate formation inside.
4. During hydrate formation in clayey silts, the clay minerals, the saline ions, the high content of fine grains (Gibbs-Thomson effect) and the high driving force (overpressure in this study) required for a critical-size hydrate core formation induced by entropy reduction, can all lead to the shift of phase boundary toward low-temperature and high-pressure condition. This phenomenon of hydrate formation hysteresis is more obvious in the clay-rich sample.
5. The impeded pressure conduction can lead to decomposition hysteresis. Pressure difference must continuously increase for initial decomposition until it can overcome the high adhesion of water by clay minerals and the high capillary force of matrix pores and throats. Hydrates in biological fossils present more remarkable decomposition hysteresis.
6. During hydrate decomposition, silty matrix gradually moves downward due to decreasing strength. For clay-rich sample, the dominant channels for decomposed water and gas will be compressed and affect productivity. While in quartz-rich reservoir, capillary interstice hinders migration of decomposed gas and water, resulting in the dispersed formation of secondary hydrate in silty matrix and the consequent discontinuous gas production.

Therefore, for clayey silt hydrate reservoirs with different mineral compositions and hydrate occurrences, both the reservoir stability and the decomposition hysteresis should be taken into consideration, and reasonable depressurization scheme should be adopted together with monitoring system. Targeted reconstruction methods should be used to impede the shrinkage or even disappearance of dominant channels and to avoid the secondary pore-filling (embedded) hydrates dispersed in fine capillary interstice. Moreover, in order to achieve long-term stable development of clayey silt hydrate reservoirs, thermal stimulation should be considered as parallel measure. The future work should focus on how the mechanical and fluid flow properties change with hydrate phase transition, which hope to be contributed to improved measures for impelling efficient development in fine-grained hydrate sediments.

Credit author statement

Hang Bian: Conceptualization, Methodology, Writing – original draft, Validation, Formal analysis; **Xuwen Qin**: Conceptualization, Investigation; **Jinsheng Sun**: Conceptualization, Investigation; **Wanjing Luo**: Conceptualization, Writing – review & editing; **Cheng Lu**: Resources, Funding acquisition; **Jian Zhu**: Experiment design, Writing – review & editing; **Chao Ma**: Writing – review & editing, Investigation; **Yingfang Zhou**: Conceptualization, Writing – review & editing.

Declaration of competing interest

The authors declare that they have no known competing financial interests or personal relationships that could have appeared to influence the work reported in this paper.

Data availability

Data will be made available on request.

Acknowledgements

The authors are grateful to the National Natural Science Foundation of China, China [51991365]; China Geological Survey Project, China [DD20211350]; Guangdong Major Project of Basic and Applied Basic Research, China [2020B0301030003]; Key Program of Marine Economy Development (Six Marine Industries) of Special Foundation of Department of Natural Resources of Guangdong Province, China [2021]56.

Appendix

A. SEM sample preparation

Firstly, the original sample was prepared precisely into a specified shape. Then, the prepared sample was dried in the oven for dry imaging. After that, the argon ion polishing instrument is utilized to polish the sample surface. The principle is that the ionized argon gas accelerates to the sample and the surface is polished by ion sputtering through momentum transfer during collision. As a result, the surfaces are smooth and parallel. And the carbon coater is finally used for protecting sample surface and improving the scanning effect of SEM.

B. Threshold segmentation and gray distribution curves

For efficient analysis, the original 16bit binary images are firstly transformed into 8bit images. Due to the great variety of minerals, the curves of various substances overlap each other. The integral gray value distribution curve of each silty matrix is shown in Fig. A.1 (A) and (B), respectively. The segmentation threshold of the two phases (solid phase and fluid phase) is determined by the watershed algorithm [108] in Avizo software. The segmented CT images are shown in the figures. The blue represents pore space and the yellow represents rock phase. The threshold value of clay-dominated clayey silt matrix is 129, and that of quartz-dominated clayey silt matrix is 69.

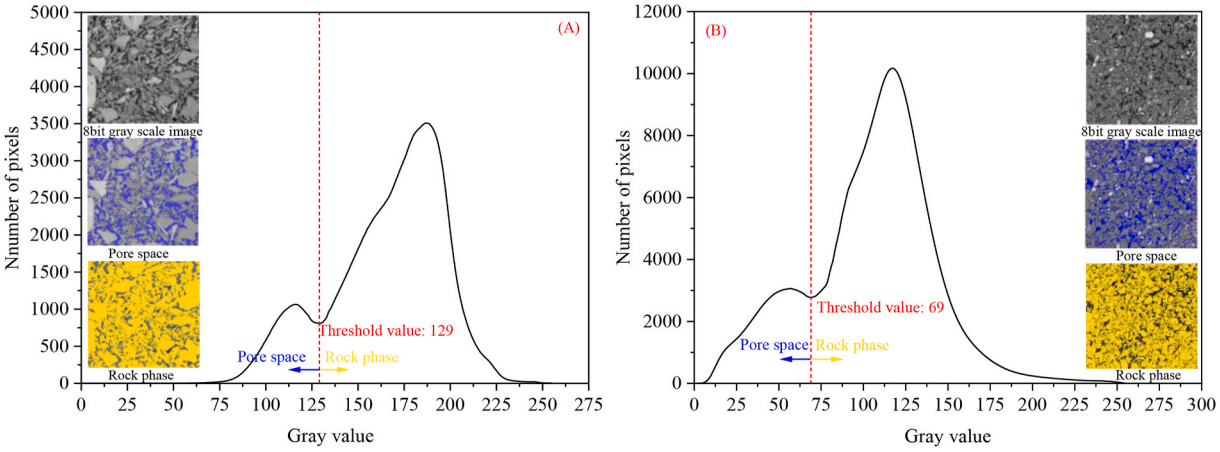

Fig. A.1. Gray value distribution corresponding to pore space and rock phase in matrix part of the clayey silt sample (A) and (B).

C. Size independence verification of the REVs shown in Fig. 7

In the silty matrix of the two clayey silt samples, 5 REVs at random positions are selected and the side length of REV (the minimum is 50 pixels) increases with an increment of 50 pixels. The maximum side length of REV in clay-dominated matrix is 500 pixels, while it is 800 pixels in quartz-dominated matrix. The curves of porosity versus side length of REV have been shown in the Fig. A.2 (A) and (B). With the increase of the side length of REV, the porosity gradually converges. The average and the variance of the porosity of REVs with different sizes are calculated. The hypothesis tests (T test and F test) are performed with the values of the maximum REVs, and the confidence interval is 95%. Detailed descriptions of the methods can refer to the research of Liu et al. [109]. Finally, the side length of the REV from clay-dominated clayey silt matrix is determined to be 300 pixels, while that of the REV from quartz-dominated clayey silt matrix is 500 pixels.

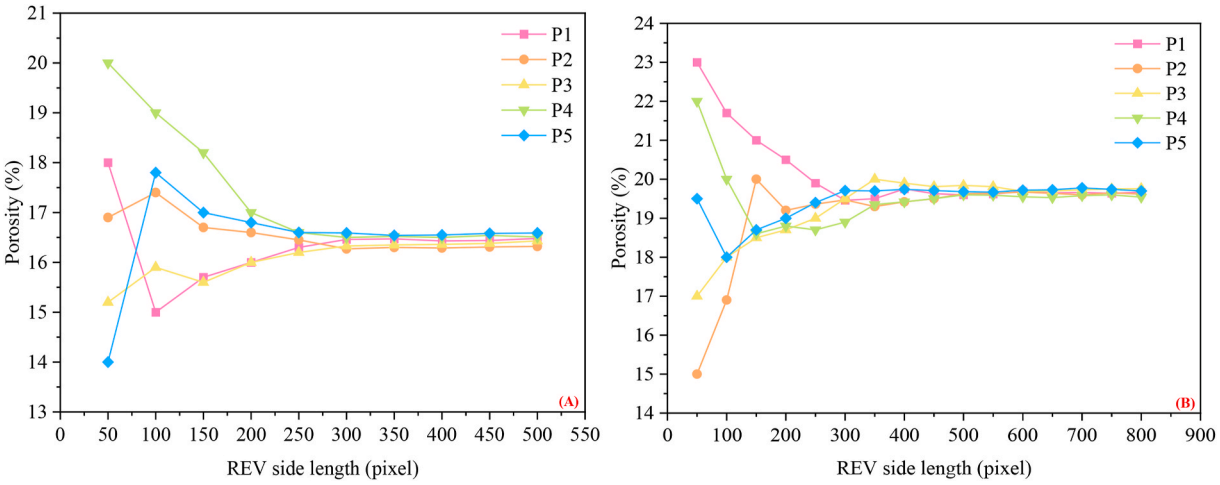

Fig. A.2. The relationship between porosity and REV side length of the silty matrix of sample (A) and (B).

References

[1] Aydin G, Karakurt I, Aydiner K. Analysis and mitigation opportunities of methane emissions. Energy Sector, Energy Sources, Part A: Recovery, Utilization, and Environmental Effects 2012;34(11):967–82. https://doi.org/10.1080/15567031003716725.

[2] Aydin G, Kaya S, Karakurt I. Modeling of coal consumption in Turkey: an application of Trend Analysis. In: 24th International mining congress and exhibition of Turkey-IMCET'15. 14–17 April. Turkey: Antalya; 2015.

[3] Jr S, Koh C. Clathrate hydrates of natural gases. third ed. New York: CRC; 2007.

[4] Moridis GJ, Collett TS, Boswell R, Kurihara M, Reagan MT, Koh C, et al. Toward production from gas hydrates: current status, assessment of resources, and simulation-based evaluation of technology and potential. SPE Reservoir Eval Eng 2009;12:745–71. https://doi.org/10.2118/114163-PA.

[5] Sloan ED. Natural gas hydrate phase equilibria and kinetics: understanding the state-of-the-art. Rev Inst Fr Pét 1990;45:245–66. https://doi.org/10.2516/ogst:1990018.

[6] Kou X, Li XS, Wang Y, Zhang Y, Chen ZY. Distribution and reformation characteristics of gas hydrate during hydrate dissociation by thermal stimulation and depressurization methods. Appl Energy 2020;277:115575. https://doi.org/10.1016/j.apenergy.2020.115575.

[7] Johnson AH. Global resource potential of gas hydrate-a new calculation. In: Proceedings of the 7th international conference on gas hydrates (ICGH 2011), edinburgh, scotland, United Kingdom; July 17-21, 2011.

[8] Qin XW, Liang QY, Ye JL, Yang L, Qiu HJ, Xie WW, et al. The response of temperature and pressure of hydrate reservoirs in the first gas hydrate production test in South China Sea. Appl Energy 2020;278:115649. https://doi.org/10.1016/j.apenergy.2020.115649.

[9] Ryu BJ, Collett TS, Riedel M, Kim GY, Chun JH, Banhk JJ, et al. Scientific results of the second gas hydrate drilling expedition in the Ulleung Basin (UBGH2). Mar Petrol Geol 2013;47:1–20. https://doi.org/10.1016/j.marpetgeo.2013.07.007.

[10] He JX, Zhong CM, Yao YJ, Yan P, Wang YL, Wan ZF, et al. The exploration and productions of gas hydrate and its research progress and exploration prospect in the northern South China Sea. Marine Geology Frontiers 2020;36(12):1–14. https://doi.org/10.16028/j.1009-2722.2020.127.

[11] Hovland M, Lysne D, Whiticar M. Gas hydrate and sediment gas composition, Hole 892A. Proceedings of the ocean drilling program, scientific results, vol. 146. Ocean Drilling Program, Texas A & M University in cooperation with the National Science Foundation and Joint Oceanographic Institutions, Inc; 1995. https://doi.org/10.2973/odp.proc.sr.146-1.210.1995. Part 1.

[12] Boswell R, Collett TS, Frye M, Shedd W, McConnell DR, Shelander D. Subsurface gas hydrates in the northern Gulf of Mexico. Mar Petrol Geol 2012;34(1):4–30. https://doi.org/10.1016/j.marpetgeo.2011.10.003.

[13] Camerlenghi A, Lucchi RG, Rothwell RG. Grain-size analysis and distribution in Cascadia Margin sediments, northeastern Pacific. Proceedings of the Ocean Drilling Program, Scientific Results. Ocean Drilling Program, Texas A & M University in cooperation with the National Science Foundation and Joint Oceanographic Institutions, Inc 1995;146(1):3–32. https://doi.org/10.2973/odp.proc.sr.146-1.202.1995. 146.

[14] von Huene RV, Suess E. Ocean drilling program leg 112, Peru continental margin: Part 1, tectonic history. Geology 1988;16(10):934–8. https://doi.org/10.1130/0091-7613(1988)016<0934: ODPLPC>2.3.CO. ;2.

[15] Kvenvolden KA, Kastner M. Gas hydrates of the Peruvian outer continental margin. Proc Ocean Drill Progr Sci Results 1990;112:517–26. https://doi.org/10.2973/odp.proc.sr.112.147.1990.

[16] Collett TS, Boswell R, Waite WF, Kumar P, Roy SK, Chopra K, et al. India national gas hydrate program expedition 02 summary of scientific results: gas hydrate systems along the eastern continental margin of India. Mar Petrol Geol 2019;108:39–142. https://doi.org/10.1016/j.marpetgeo.2019.05.023.

[17] Holbrook WS, Hoskins H, Wood WT, Stephen RA, Lizarralde D. Methane hydrate and free gas on the Blake Ridge from Vertical seismic profiling. Science 1996;273:1840–3. https://doi.org/10.1126/science.273.5283.1840.

[18] Yuan T, Hyndman RD, Spence GD, Desmons B. Seismic velocity increase and deep-sea gas hydrate concentration above a bottom-simulating reflector on the northern Cascadia continental slope. J Geophys Res Solid Earth 1996;101:13655–71. https://doi.org/10.1029/96JB00102.

[19] Matsushima J. Seismic wave attenuation in methane hydrate-bearing sediments: vertical seismic profiling data from the Nankai Trough exploratory well, offshore Tokai, central Japan. J Geophys Res Solid Earth 2006;111:B10101. https://doi.org/10.1029/2005JB004031.

[20] Shankar U, Riedel M. Gas hydrate saturation in the Krishna-Godavari basin from P-wave velocity and electrical resistivity logs. Mar Petrol Geol 2012;28(10):1768–78. https://doi.org/10.1016/j.marpetgeo.2010.09.008.

[21] Weitemeyer KA, Constable S, Tréhu AM. A marine electromagnetic survey to detect gas hydrate at Hydrate Ridge. Oregon. Geophys J Int 2011;187(1):45–62. https://doi.org/10.1111/j.1365-246X.2011.05105.x.

[22] Wang XJ, Wu SG, Lee M, Guo YQ, Yang X, Liang JQ. Gas hydrate saturation from acoustic impedance and resistivity logs in the Shenhu area, South China Sea. Mar Petrol Geol 2011;28(9):1625–33. https://doi.org/10.1016/j.marpetgeo.2011.07.002.

[23] Cortes DD, Martin AI, Yun TS, Francisca FM, Santamarina JC, Rupple C. Thermal conductivity of hydrate-bearing sediments. J Geophys Res Solid Earth 2009;114:B11103. https://doi.org/10.1029/2008JB006235.

[24] Kou X, Li XS, Wang Y, Liu JW, Chen ZY. Heterogeneity of hydrate-bearing sediments: definition and effects on fluid flow properties. Energy 2021;229:120736. https://doi.org/10.1016/j.energy.2021.120736.

[25] Wu P, Li YH, Sun X, Liu WG, Song YC. Mechanical characteristics of hydrate-bearing sediment: a review. Energ fuel 2021;35:1041–57. https://doi.org/10.1021/acs.energyfuels.0c03995.

[26] Cnudde V, Boone MN. High-resolution X-ray computed tomography in geosciences: a review of the current technology and applications. Earth Sci Rev 2013;123:1–17. https://doi.org/10.1016/j.earscirev.2013.04.003.

[27] Li CF, Hu GW, Ye YG, Liu CL, Cheng J, Zhang LK, et al. Microscopic distribution of gas hydrate in sediment determined by X-ray computerized tomography. J Optoelectron - Laser 2013;24(3):551–7.

[28] Yang L, Zhao JF, Liu WG, Li YH, Yang MJ, Song YC. Microstructure observations of natural gas hydrate occurrence in porous media using microfocus X-ray computed tomography. Energy Fuel 2015;29(8):4835–41. https://doi.org/10.1021/acs.energyfuels.5b00881.

[29] Liang HY, Guan DW, Shi KJ, Yang L, Zhang LX, Zhao JF, et al. Characterizing Mass-Transfer mechanism during gas hydrate formation from water droplets. Chem Eng J 2022;428:132636. https://doi.org/10.1016/j.cej.2021.132626.

[30] Lv JC, Cheng ZC, Xue KP, Liu Y, Mu HL. Pore-scale morphology and wettability characteristics of xenon hydrate in sand matrix-Laboratory visualization with micro-CT. Mar Petrol Geol 2020;120:104525. https://doi.org/10.1016/j.marpetgeo.2020.104525.

[31] Le TX, Bornert M, Aimedieu P, Chabot B, King A, Tang AM. An experimental investigation on methane hydrate morphologies and pore habits in sandy sediment using synchrotron X-ray computed tomography. Mar Petrol Geol 2022;122:104646. https://doi.org/10.1016/j.marpetgeo.2020.104646.

[32] Jin Y, Nagao J, Hayashi J, Shimada W, Ebinuma T, Narita H. Observation of Xe hydrate growth at gas-ice interface by microfocus X-ray Computed tomography. J Phys Chem C 2008;112:17253–6. https://doi.org/10.1021/jp803525m.

[33] Lei L, Seol Y, Choi JH, Kneafsey TJ. Pore habit of methane hydrate and its evolution in sediment matrix- Laboratory visualization with phase-contrast micro-CT. Mar Petrol Geol 2019;104:451–67. https://doi.org/10.1016/j.marpetgeo.2019.04.004.

[34] Kou X, Li XS, Wang Y, Liu JW, Chen ZY. Effects of gas occurrence pattern on distribution and morphology characteristics of gas hydrates in porous media. Energy 2021;226:120401. https://doi.org/10.1016/j.energy.2021.120401.

[35] Yang L, Falenty A, Chaouachi M, Haberthür D, Kuhs WF. Synchrotron X-ray computed microtomography study on gas hydrate decomposition in a sedimentary matrix. G-cubed 2016;17(9):3717–32. https://doi.org/10.1002/2016GC006521.

[36] Gupta A, Moridis GJ, Kneafsey TJ, Sloan ED. Modeling pure methane hydrate dissociation using a numerical simulator from a novel combination of X-ray computed tomography and macroscopic data. Energy Fuel 2009;23(12):5958–65. https://doi.org/10.1021/ef9006565.

[37] Zhang YC, Liu LL, Wang DG, Zhang Z, Li CF, Meng QG, et al. The interface evolution during methane hydrate dissociation within quartz sands and its implications to the permeability prediction based on NMR data. Mar Petrol Geol 2021;129:105065. https://doi.org/10.1016/j.marpetgeo.2021.105065.

[38] Kou X, Feng JC, Li XS, Wang Y, Chen ZY. Visualization of interactions between depressurization-induced hydrate decomposition and heat/mass transfer. Energy 2022;239:122230. https://doi.org/10.1016/j.energy.2021.122230.

[39] Rees Emily VL, Kneafsey TJ, Seol Y. Methane hydrate distribution from prolonged and repeated formation in natural and compacted sand samples: X-Ray CT observations. J Geophys Res 2011;2011:791815. https://doi.org/10.1155/2011/791815.

[40] Ecker C, Dvorkin J, Nur A. Sediments with gas hydrates; internal structure from seismic AVO. Geophysics 1998;63(5):1659–69.

[41] Dai S, Santamarina JC, Waite WF, Kneafsey TJ. Hydrate morphology: physical properties of sands with patchy hydrate saturation. J Geophys Res Solid Earth 2012;117:B11205. https://doi.org/10.1029/2012JB009667.

[42] Kou X, Li XS, Wang Y, Wan K, Chen ZY. Pore-scale analysis of relations between seepage characteristics and gas hydrate growth habit in porous sediments. Energy 2021;218:119503. https://doi.org/10.1016/j.energy.2020.119503.

[43] Helgerud MB, Dvorkin J, Nur A, Sakai A, Collett T. Elastic-wave velocity in marine sediments with gas hydrates: effective medium modeling. Geophys Res Lett 1999;26(13):2021–4. https://doi.org/10.1029/1999GL900421.

[44] Berge LI, Jacobsen KA, Solstad A. Measured acoustic wave velocities of R11 (CCl3F) hydrate samples with and without sand as a function of hydrate concentration. J Geophys Res Solid Earth 1999;104(B7):15415–24. https://doi.org/10.1029/1999JB900098.

[45] Dvorkin J, Prasad M, Sakai A, Lavoie D. Elasticity of marine sediments: rock physics modeling. Geophys Res Lett 1999;26:1781–4. https://doi.org/10.1029/1999GL900332.

[46] Syed FI, Dahaghi AK, Muther T. Laboratory to field scale assessment for EOR applicability in tight oil reservoir. Petrol Sci 2022;19(5):2131–49. https://doi.org/10.1016/j.petsci.2022.04.014.

[47] Collett TS, Johnson AH, Knapp CC, Boswell R. Natural gas hydrates: a review. In: Collett T, Jognson A, Knapp C, Boswel R, editors. Natural gas hydrates-energy resource potential and associated geologic hazards, AAPG mem, vol. 89. Vancouver: American Association of Petroleum Geologists; 2009. p. 146–219. https://doi.org/10.1306/13201142M891602.
[48] Holland M, Schultheiss PJ, Roberts J, Druce M. Observed gas hydrate morphologies in marine sediments, paper presented at 6th International Conference on Gas Hydrates, Chevron, Vancouver, B. C., Canada. 6–10 July, 2008.
[49] Wu P, Li YH, Wang L, Sun X, Wu DJ, He XF, et al. Hydrate-bearing sediment of the South China sea: microstructure and mechanical characteristics. Eng Geol 2022; 307:106782. https://doi.org/10.1016/j.enggeo.2022.106782.
[50] Liu CL, Meng QG, Hu GW, Li CF, Sun JY, He XL, et al. Characterization of hydrate-bearing sediments recovered from the Shenhu area of the South China Sea. Interpretation-J Sub 2018;5(3):SM13–23. https://doi.org/10.1190/INT-2016-0211.1.
[51] Liu CL, Meng QG, Li CF, Sun JY, He XL, Yang SX, et al. Characterization of natural gas hydrate and its deposits recovered from the northern slope of the South China Sea. Earth Sci Front 2017;24(4):41–50.
[52] Li CF, Hu GW, Zhang W, Ye YG, Lu CL, Li Q, et al. Influence of foraminifera on formation and occurrence characteristics of natural gas hydrates in fine-grained sediments from Shenhu area, South China Sea. Sci China Earth Sci 2016;59: 2223–30. https://doi.org/10.1007/s11430-016-5005-3.
[53] Bian H, Qin WX, Luo W, Ma C, Zhu J, Lu C, et al. Evolution of hydrate habit and formation properties evolution during hydrate phase transition in fractured-porous medium. Fuel 2022;324(A):124436. https://doi.org/10.1016/j.fuel.2022.124436.
[54] Badesab F, Dewangan P, Usapkar A, Kocherla M, Peketi A, Mohite K, et al. Controls on evolution of gas-hydrate system in the Krishna-Godavari basin, offshore India. G-cubed 2017;18(1):52–74. https://doi.org/10.1002/2016GC006606.
[55] Cha YH, Yun TS, Kim YJ, Lee JY, Kwon TH. Geomechanical, hydraulic and thermal characteristics of deep oceanic sandy sediments recovered during the second Ulleung Basin gas hydrate expedition. Energies 2016;9(10):775. https://doi.org/10.3390/en9100775.
[56] Liang JQ, Zhang W, Lu JA, Wei JG, Kuang ZG, He YL. Geological occurrence and accumulation mechanism of natural gas hydrates in the eastern Qiongdongnan Basin of the South China Sea: insights from Site GMGS5-W9-2018. Mar. Geol 2019;418:106042. https://doi.org/10.1016/j.margeo.2019.106042.
[57] Ye JL, Wei JG, Liang JQ, Lu JA, Lu HL, Zhang W. Complex gas hydrate system in a gas chimney, South China Sea. Mar Petrol Geol 2019;104:29–39. https://doi.org/10.1016/j.marpetgeo.2019.03.023.
[58] Johnson JE, MacLeod DR, Phillips SC, Phyllips MP, Divins DL. Primary deposition and early diagenetic effects on the high saturation accumulation of gas hydrate in a silt dominated reservoir in the Gulf of Mexico. Mar Geol 2022;444:106718. https://doi.org/10.1016/j.margeo.2021.106718.
[59] Wandrol P, Matějková J, Rek A. High resolution imaging by means of backscattered electrons in the scanning electron microscope. Mater Struct Micromech Fract 2008;567–568:313–6. https://doi.org/10.4028/www.scientific.net/MSF.567-568.313.
[60] Harding DP. Mineral identification using a scanning electron microscope. Miner Metall Process 2002;19(4):215–9. https://doi.org/10.1007/BF03403272.
[61] Bell SK, Joy KH, Pernet-Fisher JF, Hartley ME. QEMSCAN as a method of semi-automated crystal size distribution analysis: insights from Apollo 15 Mare Basalts. J Petrol 2020;61(4):egaa047. https://doi.org/10.1093/petrology/egaa047.
[62] Gottlieb P, Wilkie G, Sutherland D, Ho-Tun E, Suther S, Perera K, et al. Using quantitative electron microscopy for process mineralogy applications. JOM (J Occup Med) 2000;52(4):24–5.
[63] Inkson BJ, Mulvihill M, Mobius G. 3D determination of grain shape in a FeAl-based nanocomposite by FIB-tomography. Scripta Mater 2001;45:753–8. https://doi.org/10.1016/S1359-6462(01)01090-9.
[64] Holzer L, Indutnyi F, Gasser P, Munch B, Wegmann M. Three-dimensional analysis of porous BaTiO3 ceramics using FIB nanotomography. J Microsc 2004; 216:84–95. https://doi.org/10.1111/j.0022-2720.2004.01397.x.
[65] Prill T, Schladitz K. Simulation of FIB-SEM images for analysis of porous microstructures. Scanning 2013;35(3):189–95. https://doi.org/10.1002/sca.21044.
[66] Chaouachi M, Falenty A, Sell K, Enzmann F, Kersten M, Haberthur D, Kuhs WF. Microstructural evolution of gas hydrates in sedimentary matrices observed with synchrotron X-ray computed tomographic microscopy. G-cubed 2015;16: 1711–22. https://doi.org/10.1002/2015GC005811.
[67] Hansen TC, Falenty A, Kuhs WF. Lattice constants and expansivities of gas hydrates from 10 k up to the stability limit. J Chem Phys 2016;144:054301. https://doi.org/10.1063/1.4940729.
[68] Fu XJ, Waite WF, Cueto-Felgueroso L, Juanes R. Xenon hydrate as an analog of methane hydrate in geologic systems out of thermodynamic equilibrium. G-cubed 2019;20(5):2462–72. https://doi.org/10.1029/2019GC008250.
[69] Chen XY, Verma R, Espinoza DN, Prodanovic M. Pore-scale determination of gas relative permeability in hydrate-bearing sediments using X-ray computed microtomography and lattice Boltzmann method. Water Resour Res 2018;54(1): 600–8. https://doi.org/10.1002/2017WR021851.
[70] Hubbell JH, Seltzer SM. Tables of X-ray mass attenuation coefficients and mass energy-absorption coefficients 1 kev to 20 Mev for elements Z = 1 to 92 and 48 additional substances of dosimetric interest. NIST standard reference database 126. 1996. http://physics.nist.gov/PhysRefData/XrayMassCoef/cover.html. [Accessed 5 March 2023]. accessed.
[71] Xie YF, Lu JA, Cai HM, Deng W, Kuang ZG, Wang T, et al. The in-situ NMR evidence of gas hydrate forming in micro-pores in the Shenhu area, South China Sea. Energy Rep 2022;8:2936–46. https://doi.org/10.1016/j.egyr.2022.01.097.
[72] Zárate MA. Loess of southern south America. Quat Sci Rev 2003;22(18–19): 1987–2006. https://doi.org/10.1016/S0277-3791(03)00165-3.
[73] Francisca FM. Evaluating the constrained modulus and collapsibility of loess from standard penetration test. Int J GeoMech 2007;7(4):307–10. https://doi.org/10.1061/(ASCE)1532-3641(2007)7:4(307).
[74] Rinaldi VA, Rocca RJ, Zeballos ME. Geotechnical characterization and behavior of Argentinean collapsible loess, Character. Eng Prop Natural Soils 2007;4: 2259–86.
[75] Mozejko CA, Francisca FM. Enhanced mechanical behavior of compacted clayey silts stabilized by reusing steel slag. Construct Build Mater 2020;239:117901. https://doi.org/10.1016/j.conbuildmat.2019.117901.
[76] Liu D, Liao HL, Li YL, Meng QG, Hu GW, Wang JT, et al. Analysis of the mechanical properties of the reconstituted hydrate-bearing clayey-silt samples from the South China Sea. J Mar Sci Eng 2022;10(6):831. https://doi.org/10.3390/jmse10060831.
[77] Makogon YF, Holditch SA, Makogon TY. Natural gas-hydrates-A potential energy source for the 21st Century. J Pet Sci Eng 2007;56(1–3):14–31. https://doi.org/10.1016/j.petrol.2005.10.009.
[78] Makogon YF, Omelchenko RY. Commercial gas production from Messoyakha deposit in hydrate conditions. J Nat Gas Sci Eng 2013;11:1–6. https://doi.org/10.1016/j.jngse.2012.08.002.
[79] Toumelin E, Torres-Verdin C, Chen S. Modeling of multiple echo-time NMR measurements for complex pore geometries and multiphase saturations. SPE Reservoir Eval Eng 2003;6(4):234–43. https://doi.org/10.2118/85635-PA.
[80] Toumelin E, Torres-Verdín C, Sun B, Dunn KJ. Random-walk technique for simulating NMR measurements and 2D NMR maps of porous media with relaxing and permeable boundaries. J Magn Reson 2007;188(1):83–96. https://doi.org/10.1016/j.jmr.2007.05.024.
[81] Provis JL, Myers RJ, White CE, Rose V, van Deventer Jsj. X-ray microtomography shows pore structure and tortuosity in alkali-activated binders. Cement Concr Res 2012;42:855–64. https://doi.org/10.1016/j.cemconres.2012.03.004.
[82] Bird MB, Butler SL, Hawkes CD, Kotzer T. Numerical modeling of fluid and electrical currents through geometries based on synchrotron X-ray tomographic images of reservoir rocks using Avizo and COMSOL. Comput Geosci 2014;73: 6–16. https://doi.org/10.1016/j.cageo.2014.08.009.
[83] Liu XJ, Zhu HL, Liang LX. Digital rock physics of sandstone based on micro-CT technology. Chin J Geophys Ed 2014;57:1133–40. https://doi.org/10.6038/cjg20140411.
[84] Childs EC. Dynamics of fluids in porous media. Eng Geol 1972;7:174–5. https://doi.org/10.1016/0013-7952(73)90047-1.
[85] Wu SH, Cai ZQ, Shi SM. Oil deposit geology. Beijing: Petroleum Industry Press; 2011.
[86] Chen RS. Petroleum and gas geology. Wuhan: China University of Geosciences Press Co., LTD; 1994.
[87] Staykova DK, Kuhs WF, Salamatin AN, Hansen T. Formation of porous gas hydrates from ice powders: diffraction experiments and multistage model. J Phys Chem B 2003;107:10299. https://doi.org/10.1021/jp027787v.
[88] Lei L, Santamarina JC. Laboratory strategies for hydrate formation in fine-grained sediments. J Geophys Res Solid Earth 2018;123:2583–96. https://doi.org/10.1002/2017JB014624.
[89] Wang L, Li YH, Shen S, Liu WG, Sun X, Liu Y, et al. Mechanical behaviors of gas hydrate-bearing clayey sediments of the South China Sea. Environ Geotech 2022; 9(4):210–22. https://doi.org/10.1680/jenge.19.00048.
[90] Liu Z, Kim J, Lei L, Ning FL, Dai S. Tetrahydrofuran hydrate in clayey sediments-laboratory formation, morphology, and wave characterization. J Geophys Res Solid Earth 2019;124(4):3307–19. https://doi.org/10.1029/2018JB017156.
[91] Sun JX, Ning FL, Wu NY, Li S, Zhang K, Zhang L, et al. The effect of drilling mud properties on shallow lateral resistivity logging of gas hydrate bearing sediments. J Petrol Sci Eng 2015;127:259–69. https://doi.org/10.1016/j.petrol.2014.12.015.
[92] Jiang M, Zhu F, Utili S. Investigation into the effect of backpressure on the mechanical behavior of methane-hydrate-bearing sediments via DEM analyses. Comput Geotech 2015;69:551–63. https://doi.org/10.1016/j.compgeo.2015.06.019.
[93] Lee JY, Jung JW, Lee MH, Bahk JJ, Choi J, Ryu BJ, et al. Pressure core study of gas hydrates in the Ulleung Basin and implication for geomechanical controls on gas hydrate occurrence. Mar Petrol Geol 2013;47:85–98. https://doi.org/10.1016/j.marpetgeo.2013.05.021.
[94] Konrad JM, Morgenstern NR. Effects of applied pressure on freezing soils. Can Geotech J 1982;19:494–505. https://doi.org/10.1139/t82-053.
[95] Nixon JF. Discrete ice lens theory for frost heave in soils. Can Geotech J 1991;28: 843–59. https://doi.org/10.1139/t91-102.
[96] Chen F, Su X, Lu HF, Zhou Y. Relations between biogenic component (foraminifera) and highly saturated gas hydrates distribution from Shenhu Area, northern South China Sea. Earth Sci J China Univ Geosci 2013;38(5):907–15. https://doi.org/10.3799/dqkx.2013.089.
[97] Berge LI, Jacobsen KA, Solstad A. Measured acoustic wave velocities of R11 (CCl3F) hydrate samples with and without sand as a function of hydrate concentration. J Geophys Res 1999;104(B7):15415–24. https://doi.org/10.1029/1999JB900098.
[98] Li J, Lu JA, Kang DJ, Ning FL, Lu HF, Kuang ZG, et al. Lithological characteristics and hydrocarbon gas sources of gas hydrate-bearing sediments in the Shenhu

Area, South China sea Implications from the W01B and W02B sites. Mar Geol 2019;408:36–47. https://doi.org/10.1016/j.margeo.2018.10.013.
[99] Myerson AS. Handbook of industrial crystallization. second ed. Boston: Butterworth-Heinemann; 2002.
[100] Shimada N, Sugahara K, Sugahara T, Ohgaki K, et al. Phase transition from structure-H to structure-I in the methylcyclohexane plus xenon hydrate system. Fluid Phase Equil 2003;205(1):17–23. https://doi.org/10.1016/S0378-3812(02)00186-3.
[101] Mullin JW. Crystallization. third ed. Oxford: Butterworth-Heinmann; 2001.
[102] Park T, Lee JY, Kwon TH. Effect of pore size distribution on dissociation temperature depression and phase boundary shift of gas hydrate in various fine-grained sediments. Energy Fuel 2018;32(4):5321–30. https://doi.org/10.1021/acs.energyfuels.8b00074.
[103] Liu CL, Ye YG, Sun SC, Chen Q, Meng QG, Hu GW. Experimental studies on the P-T stability conditions and influencing factors of gas hydrate in different systems. Sci China Earth Sci 2003;56(4):594–600. https://doi.org/10.1007/s11430-012-4564-3.
[104] Ben Clennell M, Hovland M, Booth JS, Henry P, Winters WJ. Formation of natural gas hydrates in marine sediments 1. Conceptual model of gas hydrate growth conditioned by host sediment properties. J Geophys Res Solid Earth 1999;104(No. B10):22985–3003. https://doi.org/10.1029/1999JB900175.
[105] Yang MJ, Song YC, Liu Y. Effects of porous media and salinity on phase equilibrium of methane hydrates. J Dalian Univ Technolgy 2011;51(1):31–5.
[106] Xie Y, Zheng T, Zhong JR, Zhu YJ, Wang YF, Zhang Y, et al. Experimental research on self-preservation effect of methane hydrate in porous sediments. Appl Energy 2020;268:115008. https://doi.org/10.1016/j.apenergy.2020.115008.
[107] Bai DS, Zhang DW, Zhang XR, Chen GJ. Origin of self-preservation effect for hydrate decomposition: coupling of mass and heat transfer resistances. Sci Rep-UK 2015;5:14599. https://doi.org/10.1038/srep14599.
[108] Schlüter S, Sheppard A, Brown K, Wildenschild D. Image processing of multiphase images obtained via X-ray microtomography: a review. Water Resour Res 2014;50(4):3615–39. https://doi.org/10.1002/2014WR015256.
[109] Liu Y, Zhang W, Liang XL, Zu L, Tang XY. Determination on representative element volume of Nanjing silty-fine sand for its spatial pore structure. Rock Soil Mech 2019;40(7):2723–9.